LETTER

doi:10.1038/nature22796

Multilineage communication regulates human liver bud development from pluripotency

J. Gray Camp[1]*, Keisuke Sekine[2]*, Tobias Gerber[1], Henry Loeffler-Wirth[3], Hans Binder[3], Malgorzata Gac[1], Sabina Kanton[1], Jorge Kageyama[1], Georg Damm[4,5], Daniel Seehofer[4,5], Lenka Belicova[6], Marc Bickle[6], Rico Barsacchi[6], Ryo Okuda[2], Emi Yoshizawa[2], Masaki Kimura[2], Hiroaki Ayabe[2], Hideki Taniguchi[2], Takanori Takebe[2,7] & Barbara Treutlein[1,6]

Conventional two-dimensional differentiation from pluripotency fails to recapitulate cell interactions occurring during organogenesis. Three-dimensional organoids generate complex organ-like tissues[1]; however, it is unclear how heterotypic interactions affect lineage identity. Here we use single-cell RNA sequencing[2,3] to reconstruct hepatocyte-like lineage progression from pluripotency in two-dimensional culture. We then derive three-dimensional liver bud organoids[4] by reconstituting hepatic, stromal, and endothelial interactions, and deconstruct heterogeneity during liver bud development. We find that liver bud hepatoblasts diverge from the two-dimensional lineage, and express epithelial migration signatures characteristic of organ budding. We benchmark three-dimensional liver buds against fetal and adult human liver single-cell RNA sequencing data, and find a striking correspondence between the three-dimensional liver bud and fetal liver cells. We use a receptor–ligand pairing analysis and a high-throughput inhibitor assay to interrogate signalling in liver buds, and show that vascular endothelial growth factor (VEGF) crosstalk potentiates endothelial network formation and hepatoblast differentiation. Our molecular dissection reveals interlineage communication regulating organoid development, and illuminates previously inaccessible aspects of human liver development.

Recent innovations modelling human organogenesis in culture from pluripotent stem cells promise a better understanding of human

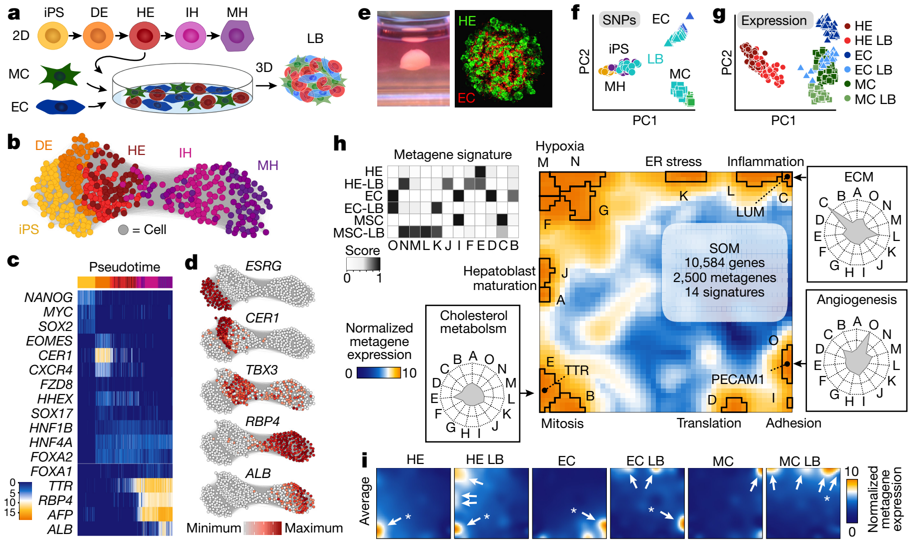

Figure 1 | Exploring human hepatic differentiation from pluripotency in 2D culture and 3D LB organoids. **a**, scRNA-seq was performed on cells during hepatocyte-like differentiation from pluripotency in 2D culture and in 3D LBs. Time points: day 0, iPS cell, 80 cells; day 6, DE, 70 cells; day 8, HE, 113 cells; day 14, IH, 81 cells; day 21, MH, 81 cells; day 0 input EC, 74 cells; day 0 input MC, 104 cells. Day 3 LBs: HE-LB, 54 cells; EC-LB, 53 cells; MC-LB, 67 cells. The 2D and 3D data are from the same two differentiation batches. Six LB replicates were analysed. **b**, Pairwise correlation lineage network reveals a differentiation topology from iPS cells through DE–HE–IH–MH. Correlation threshold, Pearson's $r > 0.4$. **c**, Pseudotime ordering of 2D cells shows changes in gene expression ($\log_2$(fragments per kilobase of mapped reads, FPKM)) from pluripotency to hepatocyte-like fate. Time point shown above the heatmap. Column, single cell; row, gene. **d**, Cell network with cells coloured on the basis of gene expression that distinguishes the lineage. **e**, Brightfield and confocal image of a 3-day LB with HE (tagged with enhanced green fluorescent protein, eGFP) and EC (Kusabira Orange, KO-Red) labelled. MCs are unlabelled. Scale bar, 100 μm. **f**, PCA separates cells on the basis of SNPs. **g**, PCA separates input and LB cells, suggesting distinct transcriptional changes upon LB formation. **h**, SOM (50 × 50 grid) constructed from input and LB single-cell transcriptomes showing scaled metagene expression. Black lines demarcate overexpressed metagene signatures. Top left heatmap shows metagene signature score for each input and LB cell population. Black represents the strongest score. ER, endoplasmic reticulum; MSC, mesenchymal stem cell. **i**, Mean profiles for each input and LB cell type are shown. Arrows mark overexpressed signatures; lineage-defining signatures (E, O, and C) are starred. See Extended Data Figs 1–5.

---

[1]Department of Evolutionary Genetics, Max Planck Institute for Evolutionary Anthropology, Deutscher Platz 6, Leipzig 04103, Germany. [2]Department of Regenerative Medicine, Yokohama City University Graduate School of Medicine, 3-9 Fukuura, Kanazawa-ku, Yokohama, Kanagawa 236-0004, Japan. [3]Interdisciplinary Centre for Bioinformatics, Leipzig University, 16 Härtelstrasse, Leipzig 04107, Germany. [4]Department of Hepatobiliary and Transplantation Surgery, University Hospital of Leipzig, Liebigstrasse 20, Leipzig 04103, Germany. [5]Saxonian Incubator for Clinical Translation (SIKT), University of Leipzig, 55 Philipp-Rosenthal-Strasse, Leipzig 04103, Germany. [6]Max Planck Institute of Molecular Cell Biology and Genetics, 108 Pfotenhauerstrasse, Dresden 01307, Germany. [7]Department of Pediatrics, Cincinnati Children's Hospital Medical Center, University of Cincinnati, 3333 Burnet Avenue, Cincinnati, Ohio 45229-3039, USA.
*These authors contributed equally to this work.

development, leading ultimately to novel human therapies[1]. A major goal in regenerative medicine is to create self-organizing human tissues, where cells experience a series of specification events that are spatially and temporally coordinated in the presence of other supporting lineages. Despite recent remarkable progress, it is unclear how the presence of diverse cells affects the identity and differentiation of each cell lineage, dampening the importance of three-dimensional (3D) multilineage organoid systems over two-dimensional (2D) monoculture approaches. Previously, we have shown that self-condensation of induced pluripotent stem (iPS) cell-derived human hepatic endoderm (HE) with supportive mesenchymal and endothelial cells results in 3D liver bud (LB)-like tissue that becomes vascularized upon transplantation into mice, and transplantation of these LBs is capable of extending life in a mouse model of liver failure[5]. Here, we set out to understand LBs by disassembling and analysing component lineages using single-cell RNA sequencing (scRNA-seq), and by doing so we learn about the processes and principles involved in human LB development.

To understand hepatic cell differentiation in the absence of supporting cells, we first analysed the transcriptional states arising during lineage programming of iPS cells to hepatocyte-like cells in 2D culture. We sequenced 425 single-cell transcriptomes from multiple time points during differentiation (Fig. 1a; day 0, iPS cells; day 6, definitive endoderm (DE); day 8, HE; day 14, immature hepatoblast-like (IH); day 21, mature hepatocyte-like (MH)), and performed principal component analysis (PCA) to identify genes that were most informative for defining cell subpopulations (Supplementary Table 1). Using these genes, we inferred lineage relationships among the cells in an adjacency network on the basis of pairwise correlations between cells (Fig. 1b)[3]. This revealed a lineage progression from iPS cells to DE, HE, IH, and MH cells with substantial heterogeneity beginning at the HE time point (Extended Data Fig. 1a–c). Heatmap visualization of gene expression with cells ordered in pseudotime revealed a temporal sequence of gene expression events during differentiation, and many cells at intermediate stages (Fig. 1c–d and Extended Data Fig. 1d, e). Notably, expression of genes maintaining pluripotency (that is, *NANOG*, *SOX2*, *MYC*) was shut down by 6 days after differentiation, and a group of genes (that is, *EOMES*, *CER1*, *CXCR4*, *FZD8*) controlling endoderm formation was upregulated by most of the day 6 cells (efficiency approaching 100%). By day 8, there was marked heterogeneity, with some cells progressing further through the lineage than others at the same time point. By day 14, nearly all cells (90%) had differentiated past DE or HE and expressed signature genes resembling a hepatoblast-like state (that is, *AFP*, *TTR*, *RBP4*). We found that DE/HE cells early in the lineage correlated with bulk RNA-seq data from embryonic day (E)8.5 mouse ventral foregut, and this correlation declined concomitantly with an increase in correlation with E10 mouse liver, reaching a maximum in IH/MH cells (Extended Data Fig. 1f). We constructed a transcription factor (TF) correlation network to visualize gene expression changes occurring during transition through the iPS cell–DE–HE–hepatocyte-like lineage, which revealed many known regulators (Extended Data Figs 1g and 2)[6–9]. Together, these data suggest that the reconstructed

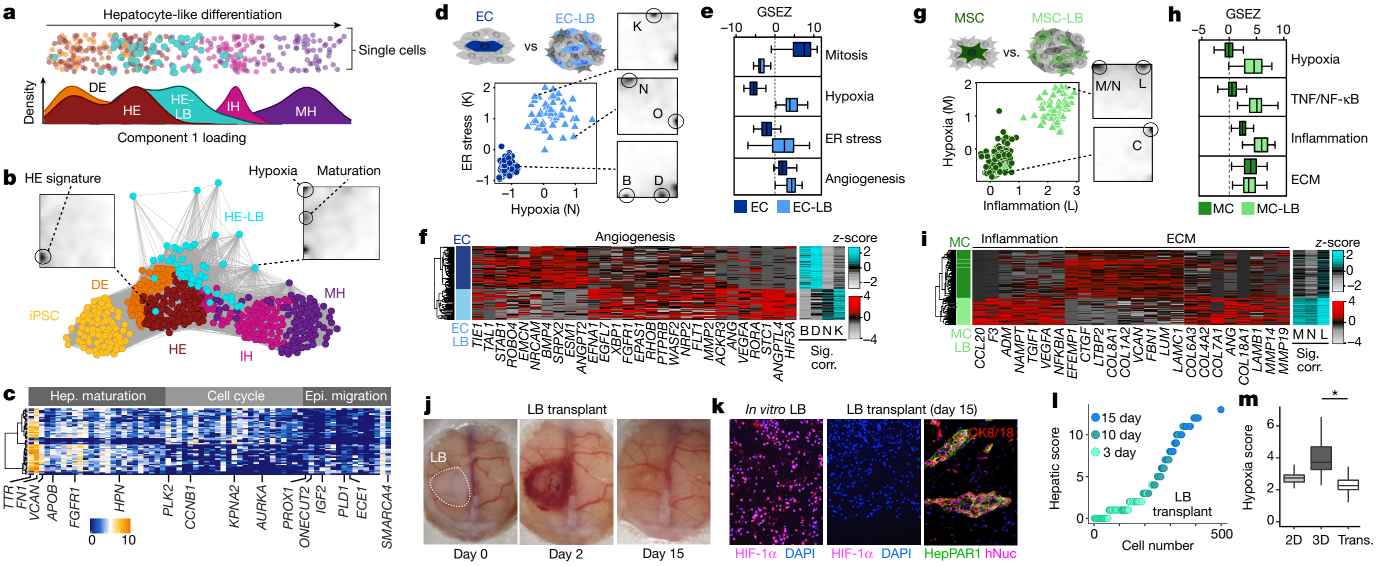

Figure 2 | Hypoxia and extracellular matrix modulation in the LB microenvironment induce hepatic outgrowth signatures and prime LBs for vascularization. a, Projection of HE-LB cells onto PC1 space from PCA of 2D hepatocyte lineage. HE-LB cells are at an intermediate stage between HE and IH. **b**, Correlation network reveals that HE-LB cells deviate from the 2D lineage. SOMs for two HE-LB cells show distinct HE-LB signatures. **c**, HE-LB cells express a hepatic outgrowth signature including genes involved in hepatoblast (Hep.) maturation, cell cycle progression, and epithelial (Epi.) migration. $\log_2$(FPKM) scale. **d**, Scatterplot showing SOM signature scores enriched for genes involved in hypoxia (N) and endoplasmic reticulum stress (K). SOM profiles are shown for representative single ECs and EC-LBs, with signatures circled. **e**, Boxplots of gene set enrichment *z*-scores (GSEZ) for mitosis, hypoxia, endoplasmic reticulum stress, and angiogenesis categories for each EC (dark blue) and EC-LB (light blue). **f**, Heatmap showing differential expression of genes involved in angiogenesis with columns scaled (*z*-score). **g**, Scatterplot showing SOM signature scores enriched for genes involved in inflammation (M) and hypoxia (L). SOM profiles are shown for representative single MC and MC-LB, with signatures circled. **h**, Boxplots of gene set enrichment *z*-scores for hypoxia, TNF/NF-κB signalling, inflammatory response, and extracellular matrix component categories in each MC (dark green) and MC-LB (light green). **i**, Heatmap showing differential expression of genes involved in inflammation and extracellular matrix columns scaled (*z*-score). **j**, Images at 0, 2, and 15 days after LB transplantation into mouse cranial window. Blood perfusion begins around 2 days and by 15 days the LB is vascularized. **k**, LB vascularization upon transplantation resolves hypoxia. Three-day LB organoid immunostained with hypoxia marker HIF-1α (magenta) and DAPI (blue). Fifteen-day LB transplant immunostained with hypoxia marker HIF-1α (magenta) and DAPI (blue), or hepatocyte marker HepPAR1 (green), epithelial CK8/18 (red), and nuclear marker hNuc(magenta). Scale bar, 100 μm. **l**, Hepatic maturation score from 84, 47, and 26 eGFP$^+$ hepatic cells 3 (teal), 10 (green), and 15 (blue) days after transplantation from scRNA-seq data. Data from two LBs per time point. **m**, Boxplots comparing hypoxia scores between 2D HE (113 cells), 3D HE-LB (54 cells), and transplanted (Trans.) LB (157 cells) hepatic cells show that hypoxia-related gene expression is reduced after transplant vascularization. Two-sided *t*-test, $^*P = 8.2 \times 10^{-16}$. See Extended Data Figs 4–7.

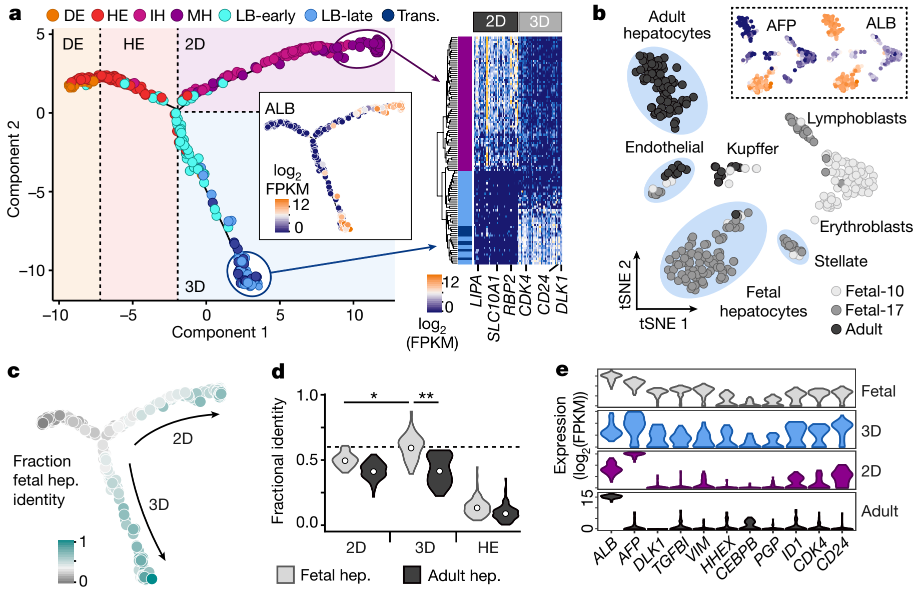

Figure 3 | A divergent hepatic lineage trajectory in the LB generates cells that resemble fetal human hepatocytes. a, Lineage reconstruction using genes identified by PCA reveals a bifurcation in 2D and 3D trajectories. Mature albumin-positive (ALB$^+$) cells accumulate in the terminus of both lineages. Heatmap shows 2D and 3D ALB$^+$ cells (rows) hierarchically clustered (Pearson) on the basis of differentially expressed genes. DE (orange) and HE (red), immature and mature 2D IH (pink) and MH (purple), early (3 days, teal) and late (6 – 12 days, light blue) time point 3D LB, and LB transplant cells (5 – 15 days, dark blue). **b**, tSNE on single-cell transcriptomes from human adult (three donors, age 21 – 65, 256 cells) and fetal (two donors, gestation weeks 10.5 and 17.5, 238 cells) liver. We identified hepatic, endothelial, mesenchymal, and immune lineage cells both in fetal and in adult tissues. ALB and α-fetoprotein (AFP) expression shown as coloured tSNE plots (log$_2$(FPKM)). Adult and fetal hepatic cells cluster separately. **c**, Quadratic programming was used to calculate the fractional identity of each 2D and 3D lineage cell's transcriptome with mock-bulk transcriptomes from DE or fetal hepatocytes (hep.). Lineage reconstruction is coloured by fetal hep. fractional identity. **d**, Adult and fetal fractional identity distributions are plotted for cells on the 2D (IH, MH) and 3D (LB-early, LB-late, transplant) lineages. The fractional identity distributions are shown for HE cells as comparison. Asterisks denote significance (Welch's two-sample *t*-test: $*P = 1 \times 10^{-10}$; $**P = 2.4 \times 10^{-5}$). **e**, Representative gene expression is shown for 2D (purple) and 3D (blue) lineage cells, and for fetal (light grey) and adult (dark grey) hepatocytes. See Extended Data Figs 7–9.

2D hepatocyte-like lineage recapitulates many aspects of *in vivo* hepatogenesis.

We next wanted to understand how a 3D microenvironment composed of HE, endothelial cell (EC) and mesenchymal cell (MC) lineages affects hepatogenesis in 3D LB organoids (Fig. 1a). Within 24 h of co-culture of these three lineages, a morphological event driven by MCs resulted in condensation into a 3D multilineage tissue (Fig. 1e)[4]. We compared a total of 465 single-cell transcriptomes of input cells (HE, ECs, MCs) with those of single cells isolated from LB organoids at an early time point (3 – 4 days of LB development, 11 – 12 days after iPSC cells). We used sequences from each input lineage (iPS cell, EC, MC) to identify single nucleotide polymorphisms (SNPs) that were informative for label-free identification of each LB cell type (Fig. 1f and Extended Data Fig. 3a, b), resulting in unambiguous identification of iPS cell-derived hepatic cells (HE-LB), ECs (EC-LB), and MCs (MC-LB). We then performed PCA on input and LB cells combined and found that principal components (PC)1–3 separated each input and LB population, revealing that each lineage undergoes transcriptional changes upon LB development (Fig. 1g and Extended Data Fig. 3c, d).

We used self-organizing maps (SOMs) to identify and visualize coordinately expressed gene groups that changed for each population during LB formation (Fig. 1f and Extended Data Figs 4 and 5). We generated a SOM by organizing 10,584 genes variably expressed in the LB and input cells into 500 metagenes and identified 14 overexpressed signatures characterizing diverse LB responses (Fig. 2c–e and Supplementary Tables 2 and 3). We discovered that LB cells maintain lineage-defining signatures found in the input populations (Fig. 1h, i and Extended Data Fig. 5h). We also identified diverse lineage-specific responses involving cell differentiation, hypoxia, endoplasmic reticulum stress, inflammation, extracellular matrix organization, and vasculogenesis, which we explore in more detail later.

HE-LB cells overexpressed signatures with enrichments for genes involved in hypoxia, epithelial cell shape and migration, phagocytosis, GTPase activation, and lipoprotein metabolism (signatures A, J, F; Fig. 1i and Extended Data Fig. 5). We projected HE-LB cells onto the principal component and intercellular correlation network spaces determined from analysis of the 2D homotypic culture (Fig. 2a, b), and found that HE-LB cells were at an intermediate maturation stage relative to HE and IH (Extended Data Fig. 6a, b). We compared HE-LB, HE, IH, and MH cells using *t*-distributed stochastic neighbour embedding (tSNE) and found that HE-LB cells clustered separately from the 2D cells and expressed distinct genes involved in cell-matrix adhesion, glycolysis, hypoxia, and cell signalling (Fig. 2b, c and Extended Data Fig. 6c, d). Interestingly, we observed substantial heterogeneity in the HE-LB population, with some cells expressing an epithelial migration signature including genes such as *PROX1* and *ONECUT2* (Extended Data Fig. 6e). These two genes are required for hepatoblast migration from the endodermal epithelium into the septum transversum mesenchyme during liver development *in vivo*[10,11]. Together, these data suggest that HE cells within the 3-day LB begin maturing towards hepatocyte fate and initiate a hepatic outgrowth program distinct from cells in a homotypic 2D culture.

LB endothelial and MCs exhibit strong transcriptome responses during LB formation. EC-LB cells heterogeneously overexpressed metagenes involved in hypoxia (signature K) and endoplasmic reticulum stress (signature N), and had lower levels of proliferation signatures (signatures B, D) (Fig. 2d, e). These signatures correlated with decreased *ANGPT2* expression, and EC-LBs expressed an alternative vasculogenic profile including upregulation of *ACKR3* (also known as *CXCR7*), *HIF3A*, *MMP2*, *ANG*, and *ANGPTL4* (Fig. 2f). These endothelial responses resembled the induction phase of ECs during liver regeneration after injury[12,13] (Extended Data Fig. 5i, j). MC-LB cells heterogeneously expressed

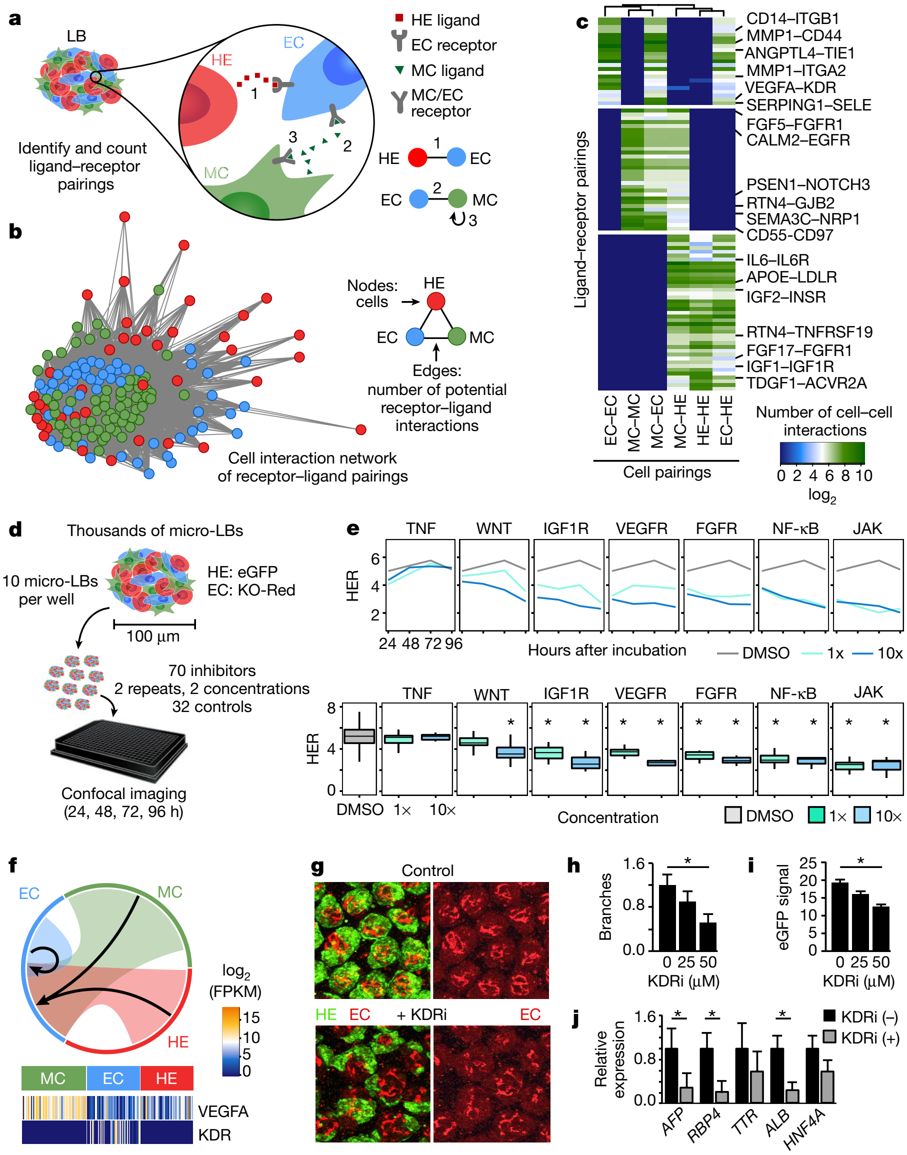

Figure 4 | Interlineage signalling affects LB development. a, Schematic showing receptor–ligand pairing screen with examples of paracrine (1, 2) and autocrine (3) interactions. **b**, Network visualizing potential cell–cell interactions in the LB. Nodes: single cells coloured by cell type; edges: sum of receptor–ligand pairings between two cells with length inversely proportional to sum. **c**, Heatmap showing the mean number of cell–cell interactions per cell type for selected receptor–ligand pairs. **d**, Experimental design of high-throughput chemical inhibition experiment. **e**, Top, the average hepatic-to-endothelial cell ratio (HER) is plotted for DMSO controls and multiple inhibitors (teal, 1 μM; blue, 10 μM) at 24, 48, 72, and 96 h after incubation. Bottom, hepatic-to-endothelial cell ratio distributions are plotted for DMSO controls and multiple inhibitors (teal, 1 μM; blue, 10 μM). Two-sided *t*-test compared with DMSO controls, $*P < 0.001$. At least ten LBs were evaluated per condition. **f**, Circle plot showing the fraction of LB cells that express VEGFA ligand mRNA linked to the fraction of cells that express the receptor KDR. Arrows designate link direction (ligand to receptor). **g**, Representative images of micro-LBs in the presence of 50 μM KDR/VEGFR2 inhibitor (KDRi; SU1498) or DMSO control. HE cells express eGFP, ECs express KO-Red. **h**, **i**, LB development is impaired in the presence of KDR inhibitor. **h**, Endothelial sprouting is quantified as mean EC branching per LB ($n = 45, 47, 51$ micro-LBs for 0, 25, and 50 μM KDR inhibitor respectively). **i**, HE composition is quantified as mean eGFP signal per micro-LB ($n = 70, 69, 68$ micro-LBs for 0, 25, and 50 μM KDR inhibitor, respectively). Two-sided *t*-test, $*P < 0.01$; error bars, s.d.; three independent differentiations. **j**, Quantitative reverse transcription PCR (qRT–PCR) for hepatoblast marker genes shows that hepatic differentiation is impaired in LBs in the presence of KDR inhibitor. Two-sided *t*-test, $*P < 0.05$; error bars, s.d.; three independent differentiations. See Extended Data Fig. 10.

hypoxia-related signatures (signatures K, M, N), which correlated with an inflammation response (signatures N, L). Nearly all MC-LBs expressed signature L, which was enriched with genes involved in tumour-necrosis factor (TNF) and nuclear factor kappa B (NF-κB) signalling (Fig. 2g, h), a pathway helping cells endure stress by inhibiting apoptosis in early LB development[14–16]. MC-LBs differentially expressed various collagens and other extracellular matrix components and upregulated matrix metalloproteinases (*MMP2*/*14*/*19*) (Fig. 2i), presumably to remodel extracellular matrix and enhance tissue permeability.

Hypoxia is known to drive angiogenesis[17]. We therefore tested whether hypoxia in the LB is resolved upon transplantation, when vasculatures form and connect with recipient circulation within 48 h (Fig. 2j). We found evidence of hypoxic stress (measured by hypoxia inducible factor 1α (HIF-1α) protein expression) in LBs *in vitro*, yet HIF-1α was low in hepatocyte clusters within transplanted LBs (Fig. 2k). We performed scRNA-seq on hepatic cells isolated from vascularized LB transplants (3, 10, and 15 days after transplantation; 157 cells total) and found that hepatic cells matured after transplantation and express *ALB* (Fig. 2l). In addition, these transplanted hepatic cells showed a reduction in hypoxic expression signatures (Fig. 2m). These data suggest that hypoxia, inflammation, and matrix remodelling in the LB microenvironment may contribute to LB vascularization upon transplantation.

To further explore hepatic cell maturation in the presence of endothelial and mesenchymal lineages, we analysed single hepatic cell transcriptomes from 3D LBs in longer-term culture *in vitro* (LB-late, 7 – 13 days in 3D, 15 – 21 days after iPS cells, 173 cells total) and after transplantation (157 cells, Extended Data Fig. 7a–c). Notably, in a lineage reconstruction using genes identified through PCA of all 2D and 3D hepatic lineage cells, we found that the 2D and 3D lineages bifurcated shortly after LB generation and continued to diverge during hepatic maturation (Fig. 3a). Cells expressing *ALB* mRNA accumulated at the terminus of the reconstruction both in 2D and in 3D lineages. Differential gene expression analysis revealed that many genes involved in mitochondrial translation, cell cycle control, cell differentiation, signalling, and cytoskeleton organization were upregulated in hepatic cells in the LB relative to the 2D monoculture (Fig. 3a and Supplementary Table 1). These data uncover parallel and divergent gene expression signatures during hepatic lineage differentiation in 2D monoculture and 3D multilineage LBs.

To understand the relevance of this divergence, we generated 494 single-cell transcriptomes from fetal (gestation weeks 10.5 and 17.5) and adult human liver (three donors, age 21, 55, and 65 years), and used tSNE to identify endothelial, mesenchymal, immune, and hepatic lineage cells from the adult and fetal tissues (Fig. 3b and Extended Data Fig. 7d–g). Fetal and adult hepatocytes clustered separately, with many genes differentially expressed between these two clusters (Supplementary Tables 1 and 4). We found that most genes specific to fetal human hepatocytes were also highly expressed in hepatoblasts freshly isolated from embryonic (E14.5 – E16.5) mouse livers (Extended Data Fig. 7h–k). We quantified the similarity between iPS cell-derived hepatocyte-like cells and the fetal or adult hepatocyte state (Extended Data Fig. 8) and found that the LB-derived hepatic cells were more similar to fetal hepatocytes than adult hepatocytes, and significantly more similar to fetal hepatocytes than all cells on the 2D lineage (Fig. 3c–e). Intriguingly, we also observed that ECs and MCs within the LB microenvironment were more similar to fetal endothelial and mesenchymal (stellate) cells than input counterparts (Extended Data Fig. 9). Altogether, these data suggest that signals in the LB promote transcriptome states that closely resemble those of human fetal cells.

ECs and MCs presented a substantial extracellular component to HE within LBs that was absent from the 2D lineage (Extended Data Fig. 10a–c). We designed an *in silico* receptor–ligand pairing screen to identify potential signalling mechanisms underlying the responses observed in the LB. We calculated the number of interactions each cell could potentially make on the basis of the presence of a complementary receptor or ligand in every other cell and summarized potential interactions in a network (Fig. 4a, b). Interestingly, MCs had the most potential interactions, and HE cells tended to interact more with MC and EC rather than with other HE cells (Extended Data Fig. 10d, e). These pairings suggest extensive crosstalk between hepatic, endothelial, and mesenchymal lineages, with many signalling pathways implicated (including TNF, fibroblast growth factor (FGF), Janus tyrosine kinase/signal transducer and activator of transcription (JAK/STAT), NF-κB, HIF, and VEGF signalling) (Fig. 4c and Extended Data Fig. 10f, g).

We pursued two strategies to test predictions from this analysis. First, we used siRNA to knockdown a receptor (TIE1) and its ligand (EDN1), which both exhibit EC-restricted expression, contribute to EC and HE pairing, and have described roles in angiogenesis[18,19] (Extended Data Fig. 10h). We generated LBs containing TIE1 or EDN1 knockdown ECs, and found that hepatic differentiation was impaired in both conditions. This shows that EC activity affects HE differentiation, and that LB organoid modularity can be exploited to study intercellular signalling. Second, we developed a high-throughput imaging approach using miniaturized LBs (100 μm diameter, hereafter called micro-LBs) to test the effect of pathway inhibition on LB development (Fig. 4d). We assayed 70 chemical inhibitors in replicate at two concentrations targeting pathways predicted from the *in silico* screen, and imaged micro-LBs at four time points (24 h, 48 h, 72 h, 96 h after incubation). Interestingly, we found that a subset of compounds decreased the ratio of hepatic to ECs compared with dimethylsulfoxide (DMSO) controls (Extended Data Fig. 10i). One example was a JAK3 inhibitor of the JAK/STAT pathway (Tasocitinib), which significantly disrupted LB integrity ($P = 1.8 \times 10^{-9}$). This was consistent with EC and mesenchymal stem cell (MSC) signatures in the LB enriched for JAK/STAT pathway components and that *JAK3* was specifically upregulated in early EC-LB cells (Extended Data Figs 5k and 10j). In general, we identified inhibitors targeting NF-κB, FGFR, IGF1R, JAK, and VEGFR pathways that had an effect on LB composition (Fig. 4e, $P < 0.001$), supporting our computational analysis that these pathways contribute to LB development.

Our receptor–ligand pairing screen and inhibitor experiment both suggested VEGF signalling as a driver of human LB development. Cells from each lineage upregulated VEGFA expression within the LB, yet only ECs expressed the receptor *KDR* (also known as *VEGFR2*) (Fig. 4f). We blocked KDR/VEGFA signalling upon co-culture of HE, EC, and MC by using a chemical KDR inhibitor (SU1498) and found that KDR inhibition did not affect self-condensation driven by MCs. However, endothelial sprouting was significantly impaired in the presence of KDR inhibitor, a response that was dose dependent (Fig. 4g, h and Extended Data Fig. 10k). In addition, KDR inhibition impaired hepatoblast abundance and differentiation (Fig. 4i, j). Interestingly, we observed no effect on hepatic differentiation when KDR was inhibited in the 2D hepatic monoculture (Extended Data Fig. 10l). This suggests that heterotypic VEGFA–KDR interactions promote hepatic differentiation specifically within LBs.

In summary, our scRNA-seq dissection of 2D and 3D hepatic differentiation reveals that both systems recapitulate certain transcriptomic features of human hepatogenesis. However, unique molecular signatures emerge during LB formation and maturation that reflect gene expression profiles found in the developing human fetal liver. Our data suggest a priming phenomenon in the LB to stimulate LB vascularization by cell-type-specific deployment of genetic programs regulating response to hypoxia[20]. This is supported by the upregulation of epithelial migration genes *PROX1* (ref. 10) and *ONECUT2* (ref. 11) in LB hepatoblasts, and matrix remodelling genes and HIF targets such as *KDR* and *VEGFA* in the mesenchymal and endothelial compartments. KDR is required for hepatic outgrowth in mice[21], and our data suggest that VEGF emanates from mesenchymal and hepatic lineages within the human LB. Given the absence of these developmentally relevant signatures in the 2D homotypic cultures, we conclude that human LB organoids model aspects of organ development and regeneration as a consequence of heterotypic interlineage communication.

Online Content Methods, along with any additional Extended Data display items and Source Data, are available in the online version of the paper; references unique to these sections appear only in the online paper.

Received 24 April 2016; accepted 27 April 2017.

1. Lancaster, M. A. & Knoblich, J. A. Organogenesis in a dish: modeling development and disease using organoid technologies. *Science* **345,** 1247125 (2014).
2. Treutlein, B. *et al.* Reconstructing lineage hierarchies of the distal lung epithelium using single-cell RNA-seq. *Nature* **509,** 371–375 (2014).
3. Camp, J. G. *et al.* Human cerebral organoids recapitulate gene expression programs of fetal neocortex development. *Proc. Natl Acad. Sci. USA* **112,** 15672–15677 (2015).
4. Takebe, T. *et al.* Vascularized and complex organ buds from diverse tissues via mesenchymal cell-driven condensation. *Cell Stem Cell* **16,** 556–565 (2015).
5. Takebe, T. *et al.* Vascularized and functional human liver from an iPSC-derived organ bud transplant. *Nature* **499,** 481–484 (2013).
6. Rankin, S. A., Kormish, J., Kofron, M., Jegga, A. & Zorn, A. M. A gene regulatory network controlling hhex transcription in the anterior endoderm of the organizer. *Dev. Biol.* **351,** 297–310 (2011).

7. Teo, A. K. *et al.* Pluripotency factors regulate definitive endoderm specification through eomesodermin. *Genes Dev.* **25,** 238–250 (2011).
8. Si-Tayeb, K. *et al.* Highly efficient generation of human hepatocyte-like cells from induced pluripotent stem cells. *Hepatology* **51,** 297–305 (2010).
9. Zaret, K. S. Regulatory phases of early liver development: paradigms of organogenesis. *Nat. Rev. Genet.* **3,** 499–512 (2002).
10. Sosa-Pineda, B., Wigle, J. T. & Oliver, G. Hepatocyte migration during liver development requires Prox1. *Nat. Genet.* **25,** 254–255 (2000).
11. Margagliotti, S. *et al.* The Onecut transcription factors HNF-6/OC-1 and OC-2 regulate early liver expansion by controlling hepatoblast migration. *Dev. Biol.* **311,** 579–589 (2007).
12. Ding, B. S. *et al.* Inductive angiocrine signals from sinusoidal endothelium are required for liver regeneration. *Nature* **468,** 310–315 (2010).
13. Hu, J. *et al.* Endothelial cell-derived angiopoietin-2 controls liver regeneration as a spatiotemporal rheostat. *Science* **343,** 416–419 (2014).
14. Zorn, A. M. in *StemBook* (2008).
15. Beg, A. A., Sha, W. C., Bronson, R. T., Ghosh, S. & Baltimore, D. Embryonic lethality and liver degeneration in mice lacking the RelA component of NF-κB. *Nature* **376,** 167–170 (1995).
16. Kamiya, A. & Gonzalez, F. J. TNF-α regulates mouse fetal hepatic maturation induced by oncostatin M and extracellular matrices. *Hepatology* **40,** 527–536 (2004).
17. Carmeliet, P. & Jain, R. K. Molecular mechanisms and clinical applications of angiogenesis. *Nature* **473,** 298–307 (2011).
18. D'Amico, G. *et al.* Tie1 deletion inhibits tumor growth and improves angiopoietin antagonist therapy. *J. Clin. Invest.* **124,** 824–834 (2014).
19. Vollmar, B. & Menger, M. D. The hepatic microcirculation: mechanistic contributions and therapeutic targets in liver injury and repair. *Physiol. Rev.* **89,** 1269–1339 (2009).
20. Dunwoodie, S. L. The role of hypoxia in development of the mammalian embryo. *Dev. Cell* **17,** 755–773 (2009).
21. Matsumoto, K., Yoshitomi, H., Rossant, J. & Zaret, K. S. Liver organogenesis promoted by endothelial cells prior to vascular function. *Science* **294,** 559–563 (2001).

Supplementary Information is available in the online version of the paper.

Acknowledgements We thank S. Pääbo, K. Köhler, A. Weigert, B. Höber, A. Weihmann, B. Vernot, K. Pfüfer, G. Renaud, M. Dannemann, J. Kelso of Max Planck Institute for Evolutionary Anthropology, M. Zerial of the Max Planck Institute of Molecular Cell Biology and Genetics, and T. Tamura, S. Tsuzuki, and C. Kaneko of Yokohama for their help with this project. This work was supported by the Max Planck Society (B.T.), PRESTO Japan Science and Technology Agency (T.T.), grants-in-aid 15H04922 and 15KK0314 from the Ministry of Education Culture and Sports of Japan (K.S.), and the AMED Research Center Network for Realization of Regenerative Medicine (H.T.). T.T. is a New York Stem Cell Foundation – Robertson Investigator.

Author Contributions T.T. and B.T. contributed equally to this work. J.G.C., K.S., B.T., and T.T. designed the study and wrote the manuscript. J.G.C. and K.S. performed single-cell experiments with assistance from T.G., S.K., B.T. and M.G. K.S., E.Y., M.K., and H.A. performed LB siRNA experiments, transplants, and stainings. R.O. performed fluorescence-activated cell sorting. G.D. and D.S. isolated human liver cells. J.G.C., B.T., and L.B. performed mouse liver scRNA-seq. J.G.C., K.S., M.B., and R.B. performed high-throughput inhibition experiments, and J.K. and J.G.C. analysed image data. H.L.W. and H.B. assisted with SOM analysis. H.T. provided financial and intellectual support.

Author Information Reprints and permissions information is available at www.nature.com/reprints. The authors declare competing financial interests: details are available in the online version of the paper. Readers are welcome to comment on the online version of the paper. Publisher's note: Springer Nature remains neutral with regard to jurisdictional claims in published maps and institutional affiliations. Correspondence and requests for materials should be addressed to B.T. (barbara_treutlein@eva.mpg.de), T.T. (Takanori.Takebe@cchmc.org), or K.S. (ksekine@yokohama-cu.ac.jp).

Reviewer Information *Nature* thanks S. Linnarsson and the other anonymous reviewer(s) for their contribution to the peer review of this work.

METHODS

No statistical methods were used to predetermine sample size. The experiments were not randomized. The investigators were not blinded to allocation during experiments and outcome assessment.

2D homotypic culture. Human iPS cell line TkDA3–4 (ref. 22) was provided by the University of Tokyo. For imaging analysis *in vitro* and *in vivo*, fluorescent protein knock-in reporter iPS cells under adeno-associated virus integration site 1 locus (AAVS1::eGFP) were used. Human umbilical vein endothelial cells (Lonza, Basel, Switzerland; CC-2517) and human MSCs (Lonza, PT-2501) were used as human ECs and MCs, respectively. Cell lines were routinely tested for mycoplasma infection using a PCR-based test (Minerva Biolabs) and were authenticated by scRNA-seq data, which supported the identity of the cell lines. Cell lines were not listed in a database of commonly misidentified cell lines maintained by the International Cell Line Authentication Committee. iPS cells were maintained on Laminin 511 E8 fragment (iMatrix-511, provided by Nippi) -coated dishes in StemFit media (Ajinomoto). To derive iPS-HE cells, we used a two-stage differentiation method combining previously published protocols[8,23,24]. Human iPS cells were seeded on a Laminin 511-E8 (iMatrix-511, Nippi) -coated dish supplemented with RPMI-1640, 1% B27 containing human 100 ng ml^{-1} activin A (Ajinomoto), and 50 ng ml^{-1} Wnt3a (R&D Systems) and cultured for 6 days to derive DE. Ten micromolar ROCK Inhibitor Y-27632 (Wako, catalogue number 253-00513) was added on the initial day of seeding. On day 6, differentiation media were added to the cells, composed of knockout-DMEM (KODMEM) containing 20% (vol/vol) knockout serum replacement, 1 mM L-glutamine, 1% (vol/vol) non-essential amino acids, 0.1 mM 2-mercaptoethanol (all from Invitrogen), and 1% (vol/vol) DMSO (Sigma). Cells were in differentiation media for 2 days to obtain HE and another 5 days to obtain IH. Finally, the cells were cultured in hepatocyte culture medium (Lonza) without EGF and supplemented with 20 ng ml^{-1} hepatocyte growth factor and 20 ng ml^{-1} oncostatinM (R&D Systems) for another 8 days. The medium was changed daily during the differentiation period. Human umbilical vein ECs and human MSCs (Lonza) were maintained in endothelial growth medium (Lonza) or MSC growth medium (Lonza) at 37 °C in a humidified 5% CO_2 incubator. Before adapting the above protocol for different iPS cell clones, we highly recommend that the respective specification markers of human iPS cells be examined at each time point of differentiation by immunostaining and gene expression studies in addition to careful microscopic observation because successful LB generation is crucial for *in vivo* functional maturation.

3D heterotypic culture. To generate human LBs *in vitro*, 1×10^6 human iPS cell-derived HE cells (day 8), 7×10^5 ECs, and 1×10^5 human MCs were resuspended in LB medium. LB medium is a mixture of endothelial growth medium and hepatocyte culture medium (Lonza) containing dexamethasone (0.1 μM, Sigma-Aldrich, St. Louis, Missouri, USA), oncostatin M (10 ng ml^{-1}, R&D System, Minneapolis, Minnesota, USA), hepatocyte growth factor (20 ng ml^{-1}, R&D Systems, Minneapolis, Minnesota, USA), and SingleQuots (Lonza), and plated on pre-solidified ×2 Matrigel diluted with endothelial growth medium (BD Biosciences, Bedford, Massachusetts, USA) in a 24-well plate. After 3–21 days of culture in LB medium, human LBs were collected and analysed or transplanted into an immunodeficient mouse.

Retroviral transduction. For live cell imaging, cells were infected with retroviruses expressing the genes encoding Kusabira-Orange fluorescent protein (KOFP) or Kusabira-Orange (KO) as described[25]. In brief, a retrovirus vector pGCDNsam IRES–eGFP or KOFP was transfected into 293gp and 293gpg packaging cells (provided by M. Onodera) in which viral particle production was induced using a tetracycline-inducible system. Culture supernatants of retrovirus-infected cells were passed through a 0.45-μm filter (Whatman, GE Healthcare, Japan) and used immediately for infection. KOFP displayed a major absorption wavelength maximum at 548 nm with a slight shoulder at 515 nm and emitted a bright orange fluorescence, with a peak at 561 nm. The *in vitro* live cell imaging was performed using a Leica TCS SP8 confocal microscope (Leica Microsystems, Germany).

Transplantation. LBs were collected after approximately 72 h of *in vitro* culture in LB medium (12 days after iPS cells, 3 days after HE induction) and transplanted into a preformed cranial window in non-obese diabetic/severe combined immunodeficient mice (Sankyo Laboratory, Tsukuba, Japan). Detailed methods are available in a published report[25]. The mice were bred and maintained according to the institutional guidelines for the use of laboratory animals.

Isolation of Dlk^{+} hepatoblasts from mouse embryonic livers. Mouse experiments were performed with institutional review board-approved protocols. Embryonic livers were dissected from pools of embryos (six to nine embryos) from timed-pregnant (E14.5, E15.5, E16.5) C57BL/6JOlaHsd mice and perfused with Liver Perfusion Medium (catalogue number 17701-038, Thermo Fisher Scientific) for 20 min in a 37 °C water bath and digested in Liver Digest Medium (catalogue number 17703-034, Thermo Fisher Scientific) supplemented with 10 μg ml^{-1} DNase I (catalogue number DN25, Sigma-Aldrich) for 20 min. Erythrocytes were lysed with Red Blood Cell Lysis Buffer (155 mM NH_4Cl, 10 mM $KHCO_3$, 0.1 mM Na_4EDTA, pH 7.4). Dlk^{+} cells were isolated using magnetic cell separation with Anti-FITC MicroBeads (catalogue number 130-048-701, Miltenyi Biotec), according to the manufacturer's protocol. Digested cells were incubated with Rat Anti-Mouse CD16/CD32 (dilution 1:100, catalogue number 553142, BD Biosciences) for 10 min; and with Anti-Dlk mAb-FITC (dilution 1:40, catalogue number D187-4, MBL) for 15 min. After washing with PBS, cells were incubated with Anti-FITC MicroBeads for 15 min and separated on a magnetic column (catalogue number 130-024-201, Miltenyi Biotec).

Adult and fetal human liver cells. All experiments were performed on human tissue obtained with the donor's informed consent. Adult human liver tissue was obtained from the Universitätsklinikum Leipzig with ethical approval from the Ethics Commission of the Medical Faculty of the University of Leipzig (approval number 177/16-lk). We used a published approach to isolate primary human hepatocytes, non-parenchymal cells (Kupffer cells), liver ECs, and hepatic stellate cells from macroscopically healthy tissue that remained from resected human liver of patients with primary or secondary liver tumours or benign local liver diseases (donor 1, female, 55; donor 2, male, 65; donor 3, male, 21). Briefly, tissue was dissociated using a two-step EGTA/collagenase P perfusion incubation. Primary human hepatocytes were separated from non-parenchymal cells by centrifugation at 50*g*. Subsequent density-gradient centrifugation steps removed dead cells and antibody panning steps were used to gather each cell fraction. Our detailed protocol has been described[26]. Fetal human liver experiments were performed with ethical approval from the Ethics Commission of the Medical Faculty of the University of the Leipzig (approval number 332/16-ek). Samples of dissociated fetal liver (10.5 and 17.5 weeks' gestation) were obtained from StemExpress, USA. The cells from the 17.5 gestational week sample contained many clumps and red blood cells and we therefore used a short-term (12 h) culture on laminin-coated plates in minimal HGM media. Healthy cells were then dissociated into a single-cell suspension and used for scRNA-seq. We performed experiments on the 10.5 gestational week sample directly after thawing cells and washing in 1× PBS.

LB immunostaining. LBs were fixed overnight at 4 °C in 4% PFA, processed, and embedded in paraffin. Transverse sections (4 μm) were placed on MAS-coated slides (Matsunami, Osaka, Japan). Immunostaining was preceded by autoclave antigen retrieval in citrate buffer (pH 6.0). The primary antibodies were anti-human: HIF-1α (BD Biosciences), and HepPAR1 and CK8.18 (both from Dako). Tissue sections were incubated with secondary antibody Alexa Fluor (Life Technologies) for 1 h at room temperature, followed by DAPI (Sigma) nuclear staining. The images were acquired using a LSM510 laser scanning microscope (Carl Zeiss, Germany).

Dissociating LBs. Whole LBs were washed three times in 1× PBS and dissociated in 2 ml of Accutase (StemPro) containing 0.2 U μl^{-1} Dnase I (Roche) for approximately 45 min, followed by serial filtering through 40, 30, and 20 μm diameter strainers to create a single-cell suspension. Cells were collected by centrifugation at 300 relative centrifugal force for 5 min and resuspended in 500 μl of organoid culture media[27]. Cell viability was assessed by Trypan blue staining (typically 85–95% viable) and counted using an automatic cell counter (Countess, ThermoFisher).

Design of scRNA-seq experiments. To understand transcriptional states arising in the 2D hepatocyte-like lineage, we performed scRNA-seq experiments at multiple time points chosen to capture known transition points (iPS cell to DE, DE to HE, HE to MH), with an intermediate time point between HE and MH (IH) to understand the maturation phase. We performed two independent differentiation experiments to control for batch effect. For the first experiment, we collected data at the iPS cell (0 days), DE (6 days), HE (9 days), IH (14 days), and MH (21 days) time points. For the second experiment, we collected data only for HE and MH time points. For LBs at an early time point, we performed scRNA-seq experiments on six LBs derived from two independent batches of LB cultures (three LBs from each batch) 12 days after differentiation from iPS cells. 2D and 3D LB data were generated from the same differentiation batch. One microfluidic chip was used per LB. In all cases, cells did not cluster by batch and batch effect did not describe most of the variation in the data. On the basis of our previous experience analysing organoid cell composition and lineage transitions during a differentiation time course, we chose a cutoff of at least 50 or more cells per time point, which should have been be sufficient to analyse heterogeneity. For LBs at later time points, we performed scRNA-seq experiments on five LBs derived from one LB batch 15, 18, 19, 20, and 21 days after differentiation from iPS cells. For transplanted LBs, we performed scRNA-seq experiments on three LBs transplanted for 3, 10, and 15 days corresponding to 14, 19, and 24 days after differentiation from iPS cells. For primary liver, scRNA-seq was performed on three adult human liver biopsies (three individuals age 21–65, two chips per individual) and two fetal liver samples (one individual each, gestational weeks 10.5 and 17.5, two chips per individual). For mouse hepatoblasts, three scRNA-seq experiments were performed on Dlk$^+$ cells from the embryonic mouse liver at three time points (E14.5, E15.5, E16.5, two chips per individual).

Capturing of single cells and preparation of complementary DNA. Single cells were captured on a medium (10 – 17 μm cell diameter) or large (15 – 25 μm cell diameter) microfluidic chip for mRNA-seq (Fluidigm) using a Fluidigm C1 system. Cells were loaded onto the chip at a concentration of 400 – 500 cells per microlitre and imaged by phase-contrast to assess the number of cells per capture site. Complementary DNA (cDNAs) were prepared on chip using a SMARTer Ultra Low RNA kit for Illumina (Clontech). ERCC (External RNA Controls Consortium) RNA spike-in Mix (Ambion, Life Technologies) was added to the lysis reaction and processed in parallel to cellular mRNA.

RNA-seq library construction and cDNA sequencing. Size distribution and concentration of single-cell cDNA were assessed by high-throughput capillary gel electrophoresis (Fragment Analyser, Advanced Analytical). Sequencing libraries were constructed in 96-well plates using an Illumina Nextera XT DNA Sample Preparation kit according to the protocol supplied by Fluidigm and as described previously[2]. Libraries were quantified by Agilent Bioanalyzer using a High Sensitivity DNA Analysis Kit as well as fluorometrically by using Qubit dsDNA HS Assay kits and a Qubit 2.0 Fluorometer (Invitrogen, Life Technologies). Up to 96 single-cell libraries were pooled and each cell was sequenced to 100 bp paired-end reads on an Illumina HiSeq 2500 to a depth of one million to five million reads. Basecalling, adaptor trimming, and de-multiplexing were performed as described[28,29].

Processing, analysis, and graphic display of scRNA-seq data. Raw reads were processed using a custom script and aligned to a Bowtie2 (ref. 30) indexed human genome (hg38 sourced from Ensembl) using TopHat[31] with default settings. Transcript levels were quantified as FPKM generated by Cufflinks[32] using gencode protein coding genes (hg38 Havana). We excluded cells that had fewer than 100,000 reads, did not express >1,000 genes, or did not express either of two housekeeping genes *ACTB* and *GAPDH*. Transcript levels were converted to the log-space by taking the $\log_2$(FPKM). R studio (https://www.rstudio.com/) was used to run custom R scripts to perform PCA (FactoMineR package), hierarchical clustering (stats package), and to construct heatmaps, correlation plots, scatter plots, violin plots, dendrograms, bar graphs, and histograms. Generally, ggplot2 and gplots packages were used to generate data graphs. The Seurat package[33] implemented in R was used to identify cell clusters and perform differential gene expression based on tSNE. The Monocle package[34] was used to analyse cell lineage relationships. Covariance network analysis and visualizations were done using igraph implemented in R (http://igraph.sf.net). Gene ontology enrichment analyses were performed using DAVID informatics Resources 6.7 (ref. 35). A list of TFs was obtained from the online 'Animal Transcription Factor Database' (http://www.bioguo.org/AnimalTFDB/; ref. 36).

Identifying LB cell types using informative SNPs. For each input cell line (iPS cell, EC, MC), mapped reads of single cells were merged and then indexed using samtools. Single base calls for chromosome 1 were collected and polymorphic sites covered by all three cell lines were merged. Informative sites were called by choosing positions where one cell line differed whereas the other two were identical. A majority assignment based on the coverage per base was used to handle heterozygous sites for each cell line. SNPs for single LB cells from the early time point were called individually as described above and compared with the informative sites reference to assign a cell type origin. We classified cells as HE, EC, or MC if the proportion of informative SNPs matching each input lineage was >70%. Cells with ambiguous calls, <70% matching with any of the three input cell types, were discarded from the analysis. This analysis also allowed us to estimate doublet rates, which averaged <10% for all early LBs.

SOMs. SOMs have been useful in analysing and visualizing high-dimensional data[37]. We developed a customizable suite of single-cell R-analysis tools (SCRAT) based on SOM machine learning to analyse cellular heterogeneity, reconstruct lineage relationships, and calculate enrichments using metagene signatures. The package will be made publicly available (http://www.treutleinlab.org) with a detailed explanation of SCRAT functionality. Details are provided in the figure-by-figure methods section below and in our previous publications[38,39]. The analyses are based on the projection of the data space into a 2D grid provided by SOM machine learning. SOM machine learning translates the high-dimensional $N \times M$ expression data matrix (N, number of genes; M, number of cells) into a $K \times M$ metadata matrix (K, number of so-called metagenes) of reduced dimensionality (for LB analysis, $N = 10{,}584$, $K = 2{,}500$; for hepatic lineage, $N = 12{,}150$, $K = 100$). Metagene expression profiles are adapted in an iterative machine learning process to optimally cover the data space once the training is completed. SOM training extracts the expression landscape of the data in terms of metagenes, each representing a cluster of co-regulated genes spatially ordered in the grid coordinate system. Our SOM method was configured to enable the robust identification of spot modules (here called signatures) inherent in the data: we used a 2D grid of size $K = 50 \times 50$ metagenes and of rectangular topology with Gaussian neighbourhood function. Details of training parameterization were described previously[38,39]. Each cell's expression landscape is described by the K metagene expression values. They are arranged according to the underlying SOM grid and visualized by an appropriate colour gradient. The colour patterns emerge as smooth textures representing the fingerprint of gene expression activity of each cell. Note that the individual portraits are mutually comparable. Population mean portraits are calculated and visualized as the mean expression value of each metagene averaged over all cells of the group (that is, HE, HE-LB, EC, EC-LB, MC, MC-LB). The SOM algorithm arranges similar metagene profiles in neighboured tiles of the map whereas more different metagenes are located more distantly. Metagenes located in the same spot-like region of the map are similarly expressed across the cells. Consequently, distinct and well-separated spots in one population collect genes of distinct expression profiles, which are concertedly over- or underexpressed in this particular population. Each spot can consequently be interpreted as a distinct expression module of a group of metagenes (which we call signatures) showing a unique expression profile in the data set studied. We define signatures by applying a simple threshold criterion selecting the metagenes of highest expression in each cell ($e^{\text{thresh}} = 0.95 \times e^{\text{max}}$). Moderate modifications of this criterion are uncritical with respect to the expression modules obtained. All signatures detected in the individual portraits are transferred into one master map to visualize the global signature patterns. Note that the detection of signature modules provides gene clusters in an unsupervised fashion without necessity for previous definition of prototypes or cluster numbers. Enrichment analysis of predefined gene sets with known biological background (Gene Ontology (GO)[40] and Hallmark annotation databases[41]) was used to assess the functional context of these expression signatures. We applied Fisher's exact test to calculate significance of over-representation of gene set members found in a particular spot compared with their random appearance. A complementary approach uses overexpression of the gene set members in the cells. Here we used the gene set z-score (GSZ score)[42], relating average expression of the gene set to overall gene expression level in a cell. This enrichment approach thus quantifies global activation of a gene set in a cell. Differential metagene expression between subgroups was evaluated using a Wilcoxon rank-sum test, and the resulting P values were translated into fdr-values[43]. P and false discovery rate values of the metagenes can be mapped into SOM grid to visualize differentially expressed regions of the portraits.

High-throughput inhibitor experiment. We generated micro-LBs by combining HE cells labelled with eGFP, ECs labelled with KO-Red, and MSCs (unlabelled) into one well of a six-well non-adherent micro-space cell culture plate (Kuraray, RB500400NA6) at a 10:7:1 ratio (approximately 1,000 cells per LB). We distributed approximately 10 micro-LBs per well of a 384-well plate and directly added DMSO or inhibitor as described in Supplementary Table 6. We cultured the LBs overnight in 37 °C 5% CO_2 and imaged the LBs at 24, 48, 72, and 96 h after incubation, changing the media and inhibitors each day. During each round of imaging, we first scanned each well under low magnification (5×) to locate objects under phase contrast; we then used automated confocal imaging (Yokogawa CellVoyager CV7000) to acquire images under 10× magnification (UPLSAPO objective, numerical aperture 0.4). Excitation was done with a 488 nm laser at 10% power, 100 ms with emission filter 525/50, a 561 nm laser at 10% power, 200 ms with emission filter 600/37, and brightfield with an LED lamp at 2% power, 200 ms with emission filter 525/50. Four series of 14-layer z-stack confocal images were acquired per well at 24 h, 48 h, 72 h, and 96 h in each of the three channels (brightfield, green, red) to LB volumes. We developed a pipeline in ImageJ to segment LBs, and quantify LB size and eGFP and KO-Red signal intensities. Segmentation was performed as follows. A Gaussian blur was applied on all images and then all z-stacks from red and green channels were merged using a max intensity projection. Auto-thresholding was performed on these images using the triangle method, followed by segmentation using the Analyze Particles plug-in (circularity = 0.05 – 1.00) with any particles touching image edges excluded from the analysis. For each particle identified, quantification of red (KO-Red) and green (eGFP) signal intensity was performed using the average pixel intensity of red and green channels respectively in each particle (LB). The hepatic-to-endothelial cell ratio was calculated by dividing green and red signal intensities. We used Welch's two-sample t-test to determine the significance between hepatic-to-endothelial cell ratio distributions between DMSO control treatment and each compound. Compounds were provided by Selleckchem.

VEGFA/KDR inhibition. For *in vitro* signal inhibition experiments, the KDR inhibitor SU1498 (Abcam) was dissolved in DMSO, and diluted in medium to final concentrations of 25 and 50 μM. LBs or micro-LBs were treated with SU1498 for 5 days. Quantification of endothelial branching and eGFP signal intensity within micro-LBs was performed blinded by the experimenter by scoring $n > 40$ micro-LBs per condition. Total RNA was extracted from three LBs from three independent differentiations ($n = 9$ LBs for each condition) by using a PureLink RNA Mini Kit (ThermoFisher). Gene expression analyses of hepatoblast specification markers were performed with a Universal probe library system (Roche) on a LightCycler480 using three technical replicates per LB.

The following qPCR primers were used. *hAFP* (NM_001134.1): probe 61 forward, TGTACTGCAGAGATAAGTTTAGCTGAC; reverse, TCCTTGTAAGTGGCTTCTTGAAC. *hRBP4* (NM_006744.3): probe 17 forward, CCAGAAGCGCAGAAGATTG; reverse, TTTCTTTCTGATCTGCCATCG. *hTTR* (NM_000371.3): probe 66 forward, GCCGTGCATGTGTTCAGA; reverse, GCTCTCCAGACTCACTGGTTTT. *hALB* (NM_000477.5) probe 27 forward, AATGTTGCCAAGCTGCTGA; reverse, CTTCCCTTCATCCCGAAGTT. *hHNF4A* (NM_000457.3): probe 27 forward, AGCAACGGACAGATGTGTGA; reverse, TCAGACCCTGAGCCACCT.

TIE1 and EDN1 knockdown. siRNA transfection was performed with Lipofectoamine RNAiMax (Thermo Fisher Scientific) according to the manufacturer's instructions. Briefly, 5×10^5 human umbilical vein ECs (LONZA, CC-2517) were seeded on 10 cm dishes. One day after plating, siRNA (final concentration 20 nM) was transfected with 30 μl of RNAiMAX. Cells were harvested 1day after transfection and used to generate micro-LBs. siRNAs targeting for TIE1, EDN1, and negative control siRNA were purchased from Thermo Fisher Scientific (Stealth RNAi). Total RNA was extracted as described above from three pools of approximately 50 micro-LBs from three independent differentiations ($n = 9$ for each condition) by using a PureLink RNA Mini Kit (ThermoFisher). Quantitative PCR was performed as described above.

Code availability. Custom code used to analyse the scRNA-seq data is provided in the Supplementary Information and details on computational aspects of each figure are provided below.

Methods for figures. Fig. 1b. We performed PCA on variable genes (variance > 0.5) expressed (> 1 FPKM) in more than two cells. We extracted the genes correlating and anti-correlating with PC1-3, using an absolute PC loading threshold > 0.2 with a maximum of 50 genes per principal component to avoid individual principal components swamping the analysis, resulting in 265 genes. To construct the cellular network, we computed a pairwise correlation matrix for all cells, using genes discovered in the PCA analysis described above. We then generated a weighted adjacency network graph using the graph.adjacency() command in igraph and visualized cells as vertices connected to other cells via edges if the Pearson pairwise correlation between two cells was higher than 0.4. The Fruchterman–Reingold layout was used to plot the network graph. To control for batch effects, we performed two independent replicates for HE and MH cells, and found that cells did not cluster by batch.

Fig. 1f, g. We performed scRNA-seq experiments on six LBs derived from two independent batches of organ bud cultures (three LBs from each batch). One microfluidic chip was used per LB. We used sequences from each input lineage (iPS cell, EC, MC) to identify SNPs that were informative for label-free identification of each LB cell type (Extended Data Fig. 3). This analysis resulted in unambiguous identification of 54 iPS cell-derived hepatic lineage cells (HE-LB), 53 ECs (EC-LB), and 67 MCs (MC-LB). We combined data from input (HE, 113 cells; EC, 74 cells; MC, 104 cells) and LB cells, and performed PCA on genes (13,722) selected for having a variance of > 0.5, expressed ($\log_2(\text{FPKM}) > 0$) in more than two cells, and correlating with at least five other genes with a Pearson correlation coefficient of > 0.3. We plotted cells according to their PC1 (variance explained $= 22.07\%$), PC2 (variance explained $= 17.12\%$), and PC3 (variance explained $= 11.96\%$) loadings using the top 50 correlating and anti-correlating genes of PC1–5 (482 genes). Note that a complementary graph is shown for PC2–3 in Extended Data Fig. 3.

Fig. 1h. We used the SCRAT package (www.treutleinlab.org) to generate a 50×50 gridded SOM using 10,584 variable genes (variance > 1) expressed ($\log_2(\text{FPKM}) > 1$) in more than two cells. We identified metagene signatures based on correlated overexpression in at least five cells (*P* value). The heatmap was scaled by weighting the metagene expression values with a linear factor scaling, amplifying the highly expressed metagenes. More details can be found in the vignettes describing the package.

Fig. 1i. We averaged all metagene expression levels for each cell of each group (HE, EC, MSC, HE-LB, MSC-LB, or EC-LB) to generate a summary expression portrait.

Fig. 2a. We used the genes from analysis of cells on the 2D hepatocyte lineage (Supplementary Table 1) and performed independent component analysis on the 2D lineage cells together with HE-LB cells. We then used density plots to visualize the distribution of IC1 loadings of cells grouped by experiment/time point. To visualize individual cells, we generated a jitter plot with cells ordered along the *x* axis on the basis of independent component 1 (IC1) loadings and with random scattering of cells along the *y* axis.

Fig. 2b. We identified genes differentially expressed between HE-LB and the other groups (HE, IH, MH) on the basis of the receiver operating characteristic test described in Extended Data Fig. 6 (Supplementary Table 1). The top 50 genes were included with the genes described in Fig. 2a (Supplementary Table 1) and used to construct the cellular network as described in Extended Data Fig. 6. Briefly, we generated a weighted adjacency network graph using the graph.adjacency() command in igraph and visualized cells as vertices connected to other cells via edges if the pairwise correlation between two cells was higher than 0.45. The Fruchterman–Reingold layout was used to plot the network graph.

Fig. 2c. For HE-LB cells only, we performed PCA on genes with a variance > 0 and an expression of $\log_2(\text{FPKM}) > 0$ in more than two cells. We extracted the genes correlating with PC2 (annotated as 'Hepatocyte maturation') and PC3 ('Cell cycle'). *ONECUT2* seemed to correlate with PC2 and anticorrelate with PC3, and was differentially expressed in HE-LB compared with the 2D lineage cells. We searched for genes that had the highest correlation with *ONECUT2* within HE-LB cells and plotted the top 20 genes in addition in this heatmap (annotated as 'Epithelial migration'). We hierarchically clustered cells on the basis of these genes and visualized their expression in a heatmap.

Fig. 2f. From the Molecular Signatures Database (MSigDB)[44] we selected genes annotated with the term 'angiogenesis' in the Hallmark and GO Biological Process collections and performed PCA on all EC and EC-LB cells using these genes. We chose the top 100 genes correlating with PC1 and PC2 and anti-correlating with PC1, intersected them with genes in signatures K, M, N, and O, and plotted a subset of the resulting genes in the presented heatmap.

Fig. 2i. From MSigDB[44] we selected the gene sets 'HALLMARK_TnfaNfkb' and 'HALLMARK_inflammatoryResponse' and performed PCA on all MC and MC-LB cells using these genes. We chose the top 50 genes correlating with PC1 and PC2 and anti-correlating with PC1, and intersected them with genes in signatures K, M, N, and O. Similarly, we identified genes annotated with the term 'extracellular matrix' in the GO Cellular Component collection that defined subpopulations of MC and MC-LB cells. We combined all genes and visualized their expression pattern across all MC and MC-LB cells in the presented heatmap.

Fig. 2l. We curated a set of marker genes highly expressed in hepatocyte-like cells (*ALB*, *AFP*, *FABP1*, *RBP4*, *TTR*, *FGG*, *FGA*, *FGB*, *APOC3*, *APOA4*, *GSTA1*, *VT*) and calculated a hepatic maturation score for each LB transplant cell by summing the genes in this list with $\log_2(\text{FPKM}) > 2$.

Fig. 2m. From MsigDB we selected the gene set 'HALLMARK_HYPOXIA' and calculated a hypoxia score for each cell by summing the genes in this list with $\log_2(\text{FPKM}) > 2$, then dividing by the sum of all expressed genes for each cell ($\log_2(\text{FPKM}) > 5$) to normalize the score across cells, and multiplying by an arbitrary factor of 1,000.

Fig. 3a. To infer lineage relationships between cells in 2D and 3D culture systems, we used Monocle2.0.0 (ref. 34) (http://cole-trapnell-lab.github.io/monocle-release/articles/v2.0.0/; default settings) to perform dimensionality reduction and lineage trajectory reconstruction by means of DDRTree, a nonlinear manifold learning algorithm. As input into Monocle, we used the expression levels of genes identified by PCA on all 2D (DE, HE, IH, MH) and 3D (HE-LB (early), HE-LB (late), transplant) cells (Supplementary Table 1, 294 genes). To identify genes differentially expressed between 2D and 3D hepatocyte-like cells, we selected all ALB$^+$ cells ($\log_2(\text{FPKM}) > 2$), and performed tSNE analysis using the Seurat package. Cells grouped into two clusters; we used Seurat's implementation of the receiver operating characteristic test to perform differential gene expression analysis between the 2D and 3D clusters, which returned classification powers and fold-change differences. We show the top differentially expressed genes with power > 0.5 (Supplementary Table 1). Pseudotime ordering of cells was established for 2D and 3D lineages using the Monocle2.0.0 trajectory analysis.

Fig. 3b. The algorithm used to cluster cells was implemented and performed using Seurat, with a cutoff of 500 expressed genes ($\log_2(\text{FPKM}) > 0$) per cell. We performed PCA to find genes that best described the heterogeneity in the data. To identify significant PCs, we performed 200 random samplings, each time randomly permuting 1% of the genes. This returned a *P* value for each gene in each PC, on the basis of how likely the gene/PC score would have been observed by chance. On the basis of this analysis, we identified six significant PCs (PC1–6; $P < 1 \times 10^{-3}$) and selected correlating and anti-correlating genes from each PC having a *P* value cutoff of $< 1 \times 10^{-3}$ with a maximum of 50 genes per PC. We performed tSNE to cluster the cells on the basis of each gene's associated PC score using the perplexity parameter $G = 2.5$. We constructed a phylogenetic tree to identify relationships between the clusters and collapsed adjacent branches where we could not identify robust differences in gene expression. We used Seurat's implementation of the receiver operating characteristic test[33] to perform differential gene expression analysis between the adjacent clusters, which returned classification powers and fold-change differences. To identify genes differentially expressed between fetal (cluster 6, Extended Data Fig. 7) and adult (cluster 3, Extended Data Fig. 7) hepatic cells, we selected genes with a fold change >2 and power >0.5.

Fig. 3c–e. See Methods for Extended Data Fig. 8

Fig. 4b. Analysis of potential receptor–ligand pairings was performed using 2,560 previously published receptor–ligand pairs[45]. An expression cutoff of $\log_2(\text{FPKM}) = 5$ was used, and only receptor–ligand pairings were considered if they contributed to 25 or more cell–cell interactions, resulting in a total of 880 receptor–ligand pairs. For each possible cell–cell combination, we summed the number of receptor ligand pairs (that is, one cell expressed the receptor and the other ligand) that connected each cell pair. We normalized the resulting cell–cell interaction matrix to the maximum number of cell–cell interactions and generated the network graph by connecting nodes (cells) at an edge threshold of 0.4 and pruned nodes that were connected to fewer than three other nodes. The network layout was set to layout.fruchterman.reingold with seed = 3.

Fig. 4c. Each receptor–ligand pair contributing to a cell–cell interaction (expression cutoff: $\log_2(\text{FPKM}) = 1$) was summed for each class of cell–cell interactions. For the heatmap, we showed the receptor–ligand pairs having a sum greater than the mean of all pairs for classes of cell–cell interaction including one (that is, HE–EC) and less than the mean for a least two.

Fig. 4f. The circlize package was used to generate the circular plot. Each of the three lineages is represented as a third of the circle. The fraction of cells expressing VEGFA ligand mRNA is highlighted and linked to the fraction of cells expressing the receptor KDR ($\log_2(\text{FPKM})$ cutoff > 1). The arrows designate the direction of the link (ligand to receptor). A subset of cells expresses both receptor and ligand.

Extended Data Fig. 1d. To infer a pseudotime order of the cells, we used Monocle[34] (default settings) to perform dimensionality reduction by means of independent component analysis and to draw a minimum spanning tree connecting the cells into a lineage. As input into Monocle, we used the expression levels of genes identified by PCA to be informative for lineage progression of cells along the iPS-MH cell lineage (Supplementary Table 1, 341 genes). Individual cells were colour-coded on the basis of experimental time point.

Extended Data Fig. 1f. We first identified genes that were differentially expressed between mouse E8.5 ventral foregut, E10.5 dorsal pancreas, E10.5 ventral pancreas, and E10.5 liver such that the $\log_2$(fold change) between any pairwise comparison was >2 (ref. 46). This resulted in 561 genes, which we sub-selected on the basis of a variance of >0.5 across single cells from DE, HE, IH, and MH time points, resulting in 310 genes. We next calculated the Spearman correlation between each cell's expression profile of these genes with each of the four bulk mouse expression profiles. We scaled correlations by mean centring and dividing by the standard deviation, and plotted the correlation for each cell as ordered on the basis of pseudotime. The data were fitted using a method-free spline.

Extended Data Fig. 1g. For the TF network analysis, we computed a pairwise correlation matrix for TFs annotated as such in the 'Animal Transcription Factor Database' (http://www.bioguo.org/AnimalTFDB/)[36] and identified those TFs with a correlation of greater than 0.3 with at least three other TFs (99 TFs). We used a permutation approach to determine the probability of finding TFs meeting this threshold by chance. We randomly shuffled the columns (TFs) of each row (cells) 500 times and calculated the pairwise correlation matrix for each permutation of the input data frame. After each permutation, we counted the number of TFs meeting our threshold. Most randomized data frames (96%) resulted in 0 TFs that met our threshold. The maximum number of TFs that met our threshold was 2, which occurred in only 0.2% of the permutations. In contrast, our data resulted in 99 TFs that met this threshold, suggesting that our threshold was strict but that all nodes and connections we present in the TF network are highly unlikely to be by chance. We used the pairwise correlation matrix for the selected TFs as input into the function graph.adjacency() of igraph implemented in R (http://igraph.sf.net) to generate a weighted network graph, in which the selected TFs were presented as vertices and all pairwise correlations >0.2 were presented as edges linking the respective vertices. The network graph was visualized using the Fruchterman–Reingold layout. TF vertices were manually colour-coded on the basis of the expression pattern along the monocle lineage. Yellow, orange, maroon, pink, and purple represent highest average expression in iPS, DE, HE, IH, and MH cells, respectively.

Extended Data Fig. 2. We expanded the TF network to non-TF genes by identifying genes that correlated with at least one TF shown in Extended Data Fig. 1 with a Pearson correlation coefficient of greater than 0.3. The network was drawn using igraph with the Fruchterman–Reingold layout, and edges were shown that linked two or fewer vertices. We assessed the likelihood of obtaining a correlation coefficient of >0.3 between a TF and another gene by chance by calculating the correlation between the 99 selected TFs and all other variable genes for our data as well as randomly permuted data. We then calculated the number of genes that had a correlation coefficient of >0.3 with at least one TF. This analysis revealed that on average about 1% of the identified genes could have met the correlation threshold by chance.

Extended Data Fig. 3. For each input cell line (iPS cell, EC, MC), mapped reads of single cells were merged and then indexed using samtools. Single base calls for chromosome 1 were collected and polymorphic sites covered by all three cell lines were merged. Informative sites were called by choosing positions where one cell line differed whereas the other two were identical. A majority assignment based on the coverage per base was used to handle heterozygous sites for each cell line. SNPs for single LB cells were called individually as described above and compared with the informative sites reference to assign a cell type origin. We classified cells as HE, EC, or MC if the proportion of informative SNPs matching each input lineage was $>70\%$. Cells with ambiguous calls, $<70\%$ matching with any of the three input cell types, were discarded from the analysis. This analysis also allowed us to estimate doublet rates, which averaged 10% for all LBs.

Extended Data Fig. 4. The SOM analysis on the 2D lineage data was performed using the SCRAT pipeline on expression of gencode protein coding genes having a variance >3. SCRAT was initialized with a 10×10 grid. More details can be found in the vignettes describing the package (http://www.treutleinlab.org).

Extended Data Fig. 5. The SOM analysis on the 3D LBs and input cell data was performed using the SCRAT pipeline on expression of gencode protein coding genes having a variance >1. SCRAT was initialized with a 50×50 grid. More details can be found in the vignettes describing the package (http://www.treutleinlab.org).

Extended Data Fig. 5h. We used the dotplot function from the Seurat package to visualize the transcript level and percentage of cells expressing a given gene.

Extended Data Fig. 5i. We calculated an induction phase score for each EC and EC-LB by determining whether each cell expressed ($\log_2(\text{FPKM}) > 5$) any of a set of genes upregulated in liver sinusoidal ECs after partial hepatosectomy from a recently published study[13]. We then counted the number of induction genes expressed and normalized by the total number of expressed ($\log_2(\text{FPKM}) > 5$) genes per cell. The plot shows the range of induction scores scaled from 0 to 1 ($\text{function}(x)((x\text{-min}(x))/(\text{max}(x)\text{-min}(x)))$).

Extended Data Fig. 6a. To construct the cellular network, we computed a pairwise correlation matrix for all cells on the 2D hepatocyte lineage (iPS cell, DE, HE, IH, MH) using genes identified by PCA and used for lineage reconstruction analysis presented in Extended Data Fig. 1 (Supplementary Table 1). We then generated a weighted adjacency network graph using the graph.adjacency() command in igraph and visualized cells as vertices connected to other cells via edges if the pairwise correlation between two cells was higher than 0.43. The Fruchterman–Reingold layout was used to plot the network graph.

Extended Data Fig. 6c. The algorithm used to cluster cells was implemented and performed with Seurat. We performed PCA to find genes that best described the heterogeneity in the data. To identify significant PCs, we performed 200 random samplings, each time randomly permuting 1% of the genes. This returned a P value for each gene in each PC, on the basis of how likely the gene/PC score would have been observed by chance. On the basis of this analysis, we identified highly significant PCs ($P < 1 \times 10^{-20}$) and selected genes from each PC with a P value cutoff of $< 1 \times 10^{-3}$ and a maximum of 50 genes per PC. We performed tSNE to cluster the cells on the basis of each gene's associated PC score using the perplexity parameter $G = 5$. We constructed a phylogenetic tree to identify relationships between the clusters and collapsed adjacent branches where we could not identify robust differences in gene expression. We used Seurat's implementation of the receiver operating characteristic test[33] to perform differential gene expression analysis between the adjacent clusters, which returned classification powers and fold-change differences.

Extended Data Fig. 7. Seurat was used for all clustering, data visualization, and marker gene identification on longer-term LB, adult and fetal human liver, and mouse embryonic liver data.

Extended Data Fig. 7a. Gencode protein coding genes with a variance cutoff of >0.5 and cells expressing 500 genes were used in the analysis. PC1–5 with maximally 50 genes per PC were used for the tSNE analysis.

Extended Data Fig. 7d. Gencode protein coding genes with a variance cutoff of >0.5 and cells expressing 500 genes were used in the analysis. PC1–6 with maximally 50 genes per PC were used for the tSNE analysis.

Extended Data Fig. 7h. A variance cutoff of >0.5 and cells expressing 500 genes were used in the analysis. PC1–3 with maximally 50 genes per PC were used for the tSNE analysis.

Extended Data Fig. 8a, b. To identify how similar single cells on the 2D and 3D *in vitro* hepatic lineages (DE, HE, IH, MH, HE-LB, all time points and transplant) were to human primary fetal or adult hepatocytes, we calculated the fractional fetal or adult human hepatocyte identity relative to a fractional DE identity for each cell. We generated mock-bulk DE, fetal hepatocyte, and adult hepatocyte transcriptomes by taking the mean expression of each gene across all cells of each group.

We then identified genes that were specifically ($\log_2$(fold change) of 3 or higher) expressed in DE versus fetal hepatocytes and in DE versus adult hepatocytes (Supplementary Table 1). We performed two separate analyses using these genes: one calculating fractional identity DE versus fetal hepatocytes, and one calculating fractional identity DE versus adult hepatocytes using quadratic programming (R package 'quadprog').

Extended Data Fig. 8d. As an alternative approach to assess similarity, we correlated each single-cell transcriptome to mock-bulk transcriptomes from adult hepatocytes, fetal hepatocytes, ALB mRNA-positive MH cells from the 2D culture, and ALB mRNA-positive cells from the 3D LBs (all genes with variance >1). The Spearman correlation coefficients were scaled for each cell in the heatmap visualization.

Extended Data Fig. 8e. Pairwise correlation (Pearson) across single cells based genes with variance >1 is visualized in the correlogram.

Extended Data Fig. 9a, e. Quadratic programming analysis was used as described for Extended Data Fig. 8. Mock-bulk transcriptomes were generated from MSCs (input MCs) and primary stellate cells (cluster 4 from Extended Data Fig. 7e), and human umbilical vein endothelial cells (input ECs) and primary endothelial cells (cluster 5 from Extended Data Fig. 7e).

Extended Data Fig. 10a, b. The Seurat package was used to cluster cells using only the expression of receptor and ligand genes with a variance cutoff >0. PC1-5 (panel A) and PC1-3 (panel B) with maximally 50 genes per PC were used for the tSNE analyses.

Extended Data Fig. 10e. Violin plots show the distribution of the edge weights in the network graph from Fig. 4b, which reflects the number of receptor–ligand pairings for each class of cell–cell interactions.

Data availability. The scRNA-seq data used in this study have been deposited in the Gene Expression Omnibus (GEO) under accession numbers GSE81252 and GSE96981. Bulk RNA-seq data from mouse foregut and liver were downloaded from the GEO under accession number GSE40823. The source code used to generate and analyse SOMs (Figs 1 and 2 and Extended Data Figs 4 and 5) is available in the Supplementary Information with updates available at http://www.treutleinlab.org/scrat-single-cell-r-analysis-toolkit/. Raw confocal image files used in the high-throughput inhibitor experiment (Fig. 4) that support the findings of this study are available from the corresponding authors upon reasonable request.

22. Takayama, N. *et al.* Transient activation of c-MYC expression is critical for efficient platelet generation from human induced pluripotent stem cells. *J. Exp. Med.* **207,** 2817–2830 (2010).
23. Loh, K. M. *et al.* Efficient endoderm induction from human pluripotent stem cells by logically directing signals controlling lineage bifurcations. *Cell Stem Cell* **14,** 237–252 (2014).
24. Kajiwara, M. *et al.* Donor-dependent variations in hepatic differentiation from human-induced pluripotent stem cells. *Proc. Natl Acad. Sci. USA* **109,** 12538–12543 (2012).
25. Takebe, T. *et al.* Generation of a vascularized and functional human liver from an iPSC-derived organ bud transplant. *Nat. Protocols* **9,** 396–409 (2014).
26. Kegel, V. *et al.* Protocol for isolation of primary human hepatocytes and corresponding major populations of non-parenchymal liver cells. *J. Vis. Exp.* **109,** e53069 (2016).
27. Lancaster, M. A. & Knoblich, J. A. Generation of cerebral organoids from human pluripotent stem cells. *Nat. Protocols* **9,** 2329–2340 (2014).
28. Renaud, G., Kircher, M., Stenzel, U. & Kelso, J. freelbis: an efficient basecaller with calibrated quality scores for Illumina sequencers. *Bioinformatics* **29,** 1208–1209 (2013).
29. Renaud, G., Stenzel, U., Maricic, T., Wiebe, V. & Kelso, J. deML: robust demultiplexing of Illumina sequences using a likelihood-based approach. *Bioinformatics* **31,** 770–772 (2015).
30. Langmead, B. & Salzberg, S. L. Fast gapped-read alignment with Bowtie 2. *Nat. Methods* **9,** 357–359 (2012).
31. Trapnell, C., Pachter, L. & Salzberg, S. L. TopHat: discovering splice junctions with RNA-Seq. *Bioinformatics* **25,** 1105–1111 (2009).
32. Trapnell, C. *et al.* Transcript assembly and quantification by RNA-Seq reveals unannotated transcripts and isoform switching during cell differentiation. *Nat. Biotechnol.* **28,** 511–515 (2010).
33. Macosko, E. Z. *et al.* Highly parallel genome-wide expression profiling of individual cells using nanoliter droplets. *Cell* **161,** 1202–1214 (2015).
34. Trapnell, C. *et al.* The dynamics and regulators of cell fate decisions are revealed by pseudotemporal ordering of single cells. *Nat. Biotechnol.* **32,** 381–386 (2014).
35. Huang, W., Sherman, B. T. & Lempicki, R. A. Systematic and integrative analysis of large gene lists using DAVID bioinformatics resources. *Nat. Protocols* **4,** 44–57 (2008).
36. Zhang, H. M. *et al.* AnimalTFDB: a comprehensive animal transcription factor database. *Nucleic Acids Res.* **40,** D144–D149 (2012).
37. Kim, D. H. *et al.* Single-cell transcriptome analysis reveals dynamic changes in lncRNA expression during reprogramming. *Cell Stem Cell* **16,** 88–101 (2015).
38. Wirth, H., Löffler, M., von Bergen, M. & Binder, H. Expression cartography of human tissues using self organizing maps. *BMC Bioinformatics* **12,** 306 (2011).
39. Wirth, H., von Bergen, M. & Binder, H. Mining SOM expression portraits: feature selection and integrating concepts of molecular function. *BioData Min.* **5,** 18 (2012).
40. Ashburner, M. *et al.*; The Gene Ontology Consortium. Gene Ontology: tool for the unification of biology. *Nat. Genet.* **25,** 25–29 (2000).
41. Liberzon, A. *et al.* The Molecular Signatures Database (MSigDB) hallmark gene set collection. *Cell Syst.* **1,** 417–425 (2015).
42. Törönen, P., Ojala, P. J., Marttinen, P. & Holm, L. Robust extraction of functional signals from gene set analysis using a generalized threshold free scoring function. *BMC Bioinformatics* **10,** 307 (2009).
43. Strimmer, K. fdrtool: a versatile R package for estimating local and tail area-based false discovery rates. *Bioinformatics* **24,** 1461–1462 (2008).
44. Subramanian, A. *et al.* Gene set enrichment analysis: a knowledge-based approach for interpreting genome-wide expression profiles. *Proc. Natl Acad. Sci. USA* **102,** 15545–15550 (2005).
45. Ramilowski, J. A. *et al.* A draft network of ligand-receptor-mediated multicellular signalling in human. *Nat. Commun.* **6,** 7866 (2015).
46. Rodríguez-Seguel, E. *et al.* Mutually exclusive signaling signatures define the hepatic and pancreatic progenitor cell lineage divergence. *Genes Dev.* **27,** 1932–1946 (2013).
47. Scialdone, A. *et al.* Computational assignment of cell-cycle stage from single-cell transcriptome data. *Methods* **85,** 54–61 (2015).

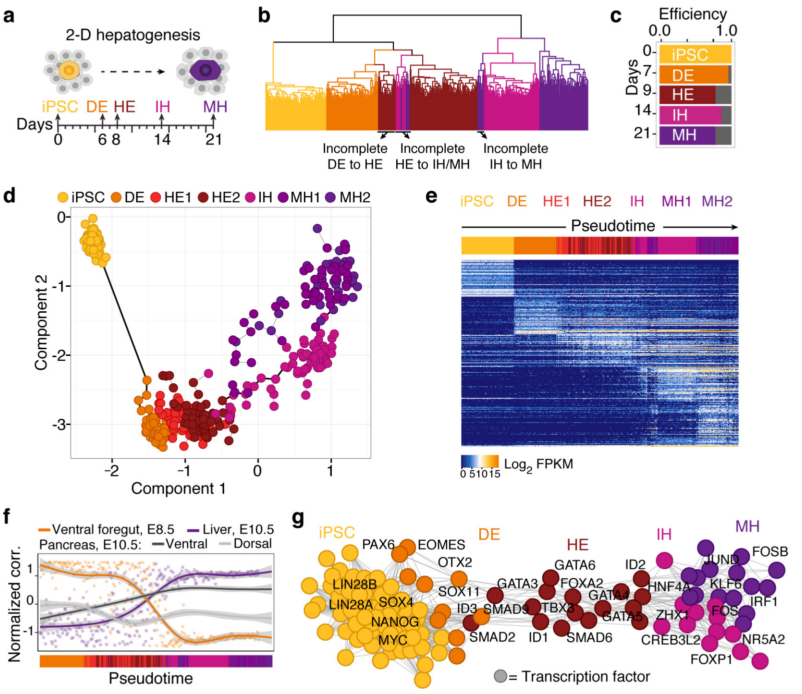

Extended Data Figure 1 | Characterizing hepatocyte-like lineage progression. a, Schematic showing time points for scRNA-seq experiments performed on iPS, DE, HE, IH, and MH cells during 2D hepatogenesis. **b**, Hierarchical clustering was performed on genes identified by PCA and is shown in **e**. Intermixing of cells from later time points with earlier time points was used to calculate the efficiency of lineage progression shown in **c**. **c**, Lineage progression efficiency at each time point shows the percentage of cells that cluster with cells from previous time points (grey). **d**, Monocle reveals hepatocyte-like lineage progression. Cells (circles, coloured on the basis of time point) are arranged in the 2D independent component space on the basis of genes identified through PCA (Supplementary Table 1). The minimum spanning tree (grey lines) connects cells, with the black line indicating the longest path. **e**, Ordering of scRNA-seq expression data according to the pseudotemporal position along the lineage reveals a continuum of gene expression changes from pluripotency to hepatocyte-like fate. Each column represents a single cell, each row a gene. The time point is shown as sidebar. **f**, Correlating cells with microdissected E8.5 ventral foregut (orange) or E10.5 ventral pancreas (dark grey), dorsal pancreas (light grey), or liver (purple) shows that transitions observed *in vitro* reflect *in vivo* development. Cells are ordered on the basis of pseudotime. **g**, Transcription factor correlation network during hepatoblast lineage progression. Shown are nodes (TFs) with more than three edges, with each edge representing a high correlation (>0.3) between connected TFs. For a full list of network TFs, see Supplementary Table 1.

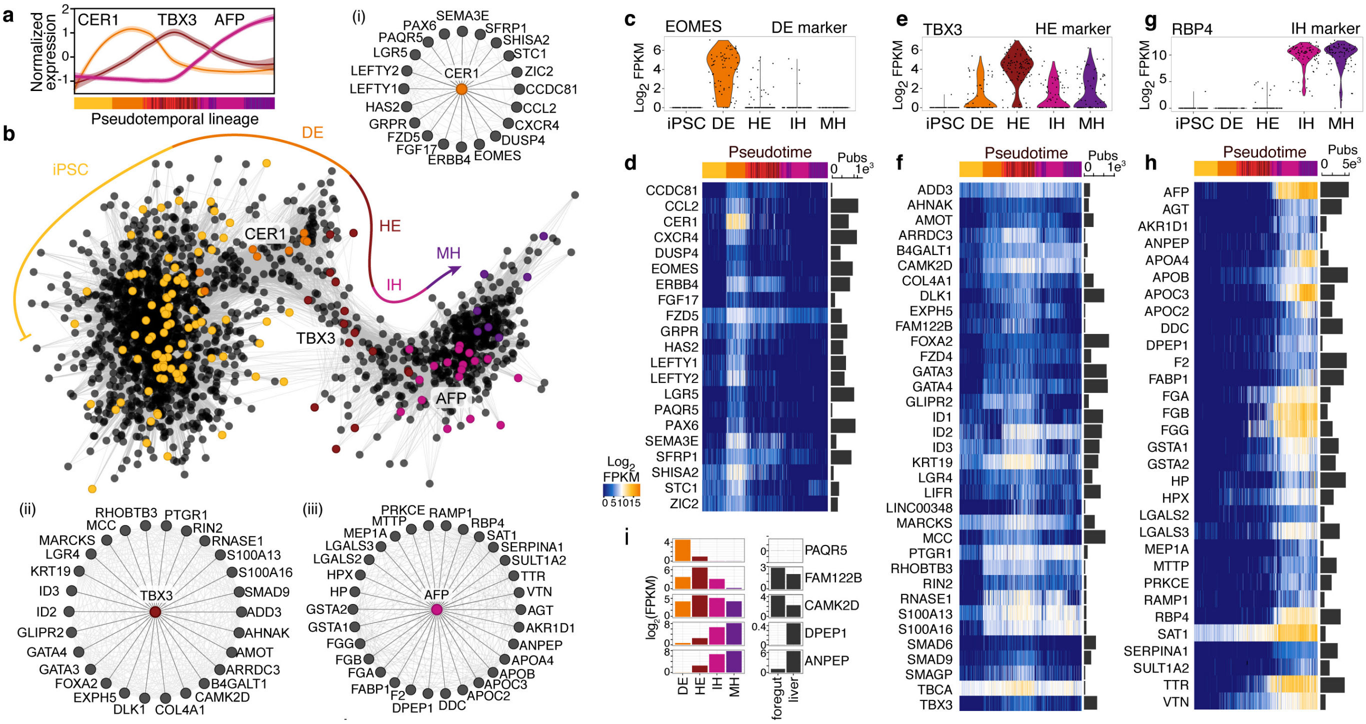

Extended Data Figure 2 | Identifying gene expression programs controlling hepatic differentiation in 2D. a, Normalized expression of three genes shows examples of dynamic gene expression along the hepatocyte lineage. Cells are ordered according to Monocle pseudotime. **b**, Covariation network using genes that have high correlation (>0.3) with TFs controlling the hepatocyte-like lineage. TF nodes are coloured according to the time point of maximal expression. Nearest neighbour subnetworks for (1) CER1, (2) TBX3, and (3) AFP show genes that strongly correlated with these known DE, HE, and hepatoblast marker genes. See Fig. 1f for base TF network. **c–h**, Violin plots and expression of subnetwork genes in cells ordered by Pseudotome. Barplots show the number of citations for each gene co-occurring with either 'liver', 'hepatogenesis', or 'endoderm' in PubMed abstracts and suggests known and novel genes involved in hepatocyte development. **i**, Expression of multiple genes with no described role in liver development in mouse E8.5 foregut and E10.5 liver confirms that these genes are dynamically expressed during liver development.

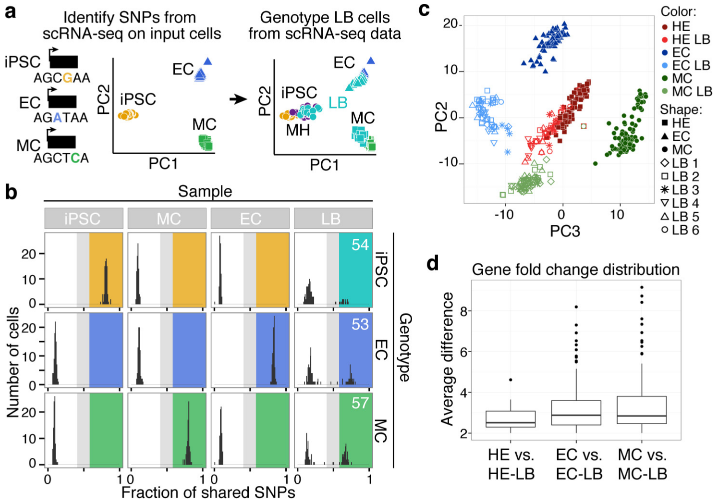

Extended Data Figure 3 | Genotyping LB cells using informative SNPs derived from scRNA-seq of input cells. a, **b**, iPS cells, ECs, and MCs used in this study were from different humans. Single-cell RNA-seq reads from iPS cells, ECs, and MCs were used to identify informative SNPs that were present in one human but not the others. Each LB cell was then genotyped on the basis of PCA clustering (**a**) and the fraction of shared SNPs with each input lineage (**b**). **c**, PCA separated each input and LB lineage, suggesting that each lineage undergoes distinct transcriptional changes upon co-culture. PCA was performed on all single-cell transcriptomes using genes expressed in more than two cells and with a non-zero variance. **d**, Boxplots showing average $\log_2$(fold-change distributions) for pairwise comparisons between 2D cultures of hepatic ectoderm, ECs, and MCs with their LB counterparts.

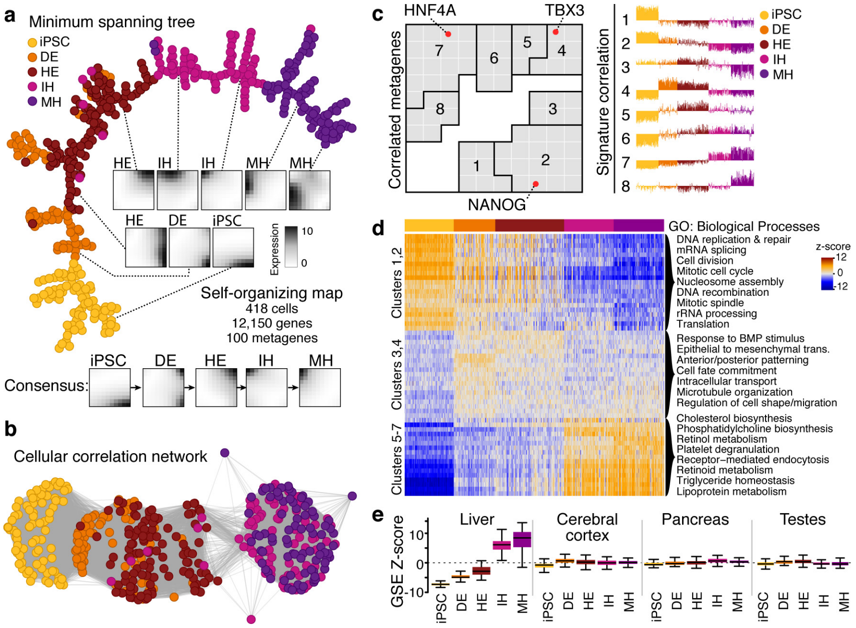

Extended Data Figure 4 | SOM metagenes reconstruct hepatocyte-like lineage progression. a, SOM analysis of 418 hepatic lineage cells using 12,150 genes organized into 100 metagenes was used to reconstruct lineage relations on the basis of a minimum spanning tree. Shown are representative single-cell portraits as well as the consensus portrait for each time point. Portraits are linearly scaled, amplifying higher expressed metagenes. **b**, Lineage network constructed from pairwise correlations between cells on the basis of the expression of 100 metagenes shows a differentiation topology from iPS cells to DE–HE–IH–MH cells, similar to Fig. 1b. **c**, Metagenes were clustered into signatures on the basis of their correlation across the cells. Each cell's correlation with each signature is shown to the right. **d**, Gene set enrichment analysis was done using genes composing each metagene signature. Top scoring enrichments for clusters 1–2, clusters 3–4, and clusters 5–7 are shown. Dark orange and blue represent a strong and weak correlation for each cell, respectively. **e**, Boxplots show gene set enrichment (GSE) distributions for each time point using curated sets of genes with specific expression in liver, cerebral cortex, pancreas, or testes.

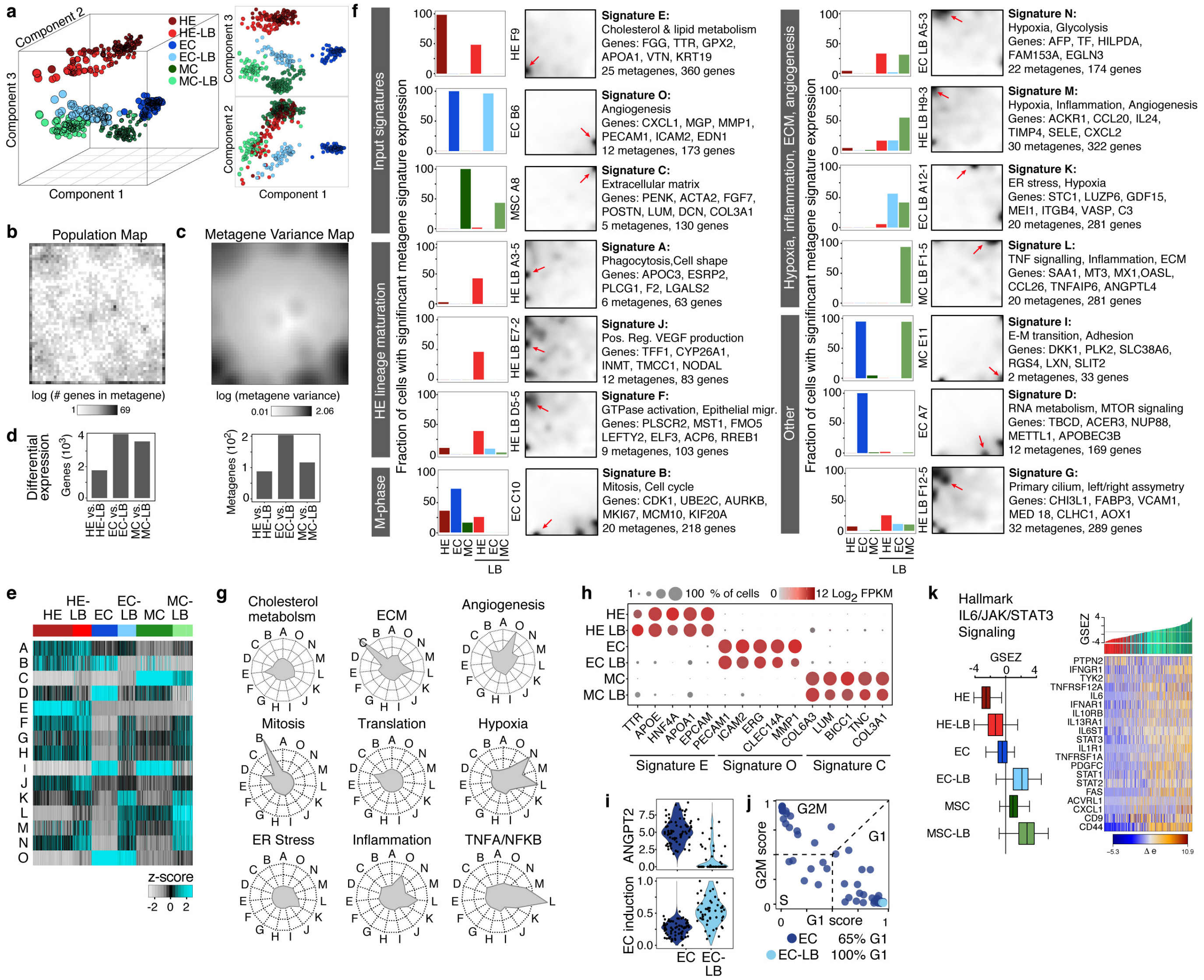

Extended Data Figure 5 | Exploring metagene signature shifts in LBs. **a**, PCA based on the expression of 2,500 metagenes separates each input and LB lineage. **b**, Population map showing the number of genes located in each metagene. **c**, Map showing the variance for each metagene across all single cells. **d**, Bar plot showing the proportion of genes and metagenes that are differentially expressed between input and LB populations. **e**, Heatmap showing normalized overexpression scores for each cell for each signature. **f**, Representative single-cell maps are shown for each overexpression signature. Bar plots show the percentage of cells from each group that display significant metagene signature expression. Each metagene signature is annotated with GO enrichments, representative genes, and the number of genes and metagenes constituting the signature. **g**, Radar plots show enrichments for genes involved in cholesterol metabolism, extracellular matrix, angiogenesis, mitosis, translation, hypoxia, endoplasmic reticulum stress, inflammation, and TNF/NF-κB signalling for each signature. Hallmark gene sets were sourced from MSigDB. **h**, Dot plot shows the expression of genes differentially expressed in HE-LB, where the size of the circle represents the proportion of cells expressing the gene and the colour represents the average expression level of each gene. **i**, Violin plot shows the distribution of scores for each EC and EC-LB cell on the basis of the expression of genes upregulated during the angiogenic induction phase of liver sinusoidal ECs after partial hepatectomy[13]. **j**, Assignment of cell cycle stage for each EC and EC-LB cell[47]. Note that 100% of EC-LB cells were scored in the G1 phase of the cell cycle. **k**, Boxplots show normalized gene set enrichment scores for the Hallmark IL6/JAK/STAT3 signalling pathway for each input and LB cell. Heatmap shows the expression of genes in this Hallmark pathway. Expression is scaled across genes. Top sidebar shows the cell type with the gene set enrichment *z*-score for each cell above. HE (light red), HE-LB (dark red), EC (dark blue), EC-LB (light blue), MC (dark green), and MC-LB (light green).

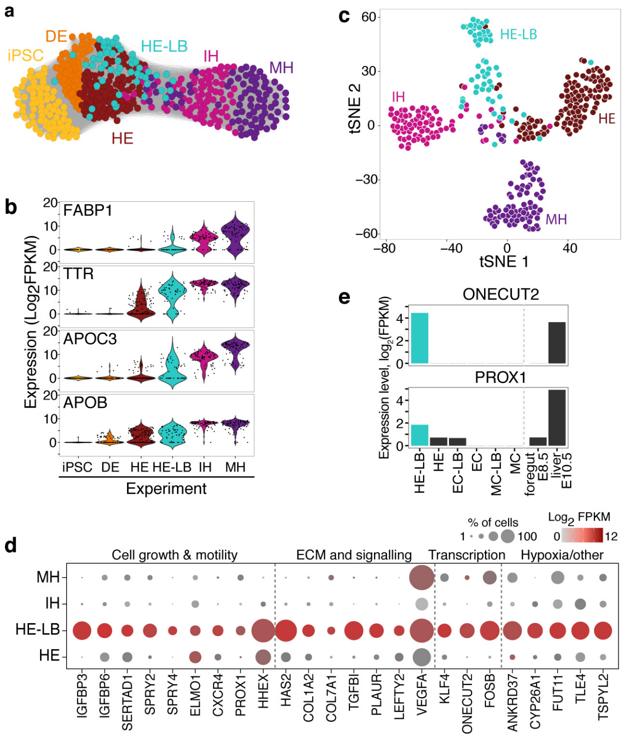

Extended Data Figure 6 | HE cells within the LB start to mature and express genes involved in hepatic outgrowth. a, Progressive differentiation of HE cells towards hepatoblast within the LB was confirmed in an intercellular correlation network using all genes used to construct the correlation network (Fig. 1). **b**, Violin plots showing the distribution of marker gene expression that are upregulated during the transition from HE to IH/MH, confirming that HE-LB cells are at intermediate stages of maturation. **c**, PCA followed by tSNE shows that many HE-LB cells have gene expression profiles different from cells on the 2D hepatocyte lineage, suggesting that cells have distinct transcriptional responses during LB self-organization. **d**, Dot plot shows the expression of genes differentially expressed in HE-LB, where the size of the circle represents the proportion of cells expressing the gene and the colour represents the average expression level of each gene. **e**, *ONECUT2* and *PROX1*, genes involved in hepatic outgrowth, are upregulated specifically in HE-LB and in E10.5 mouse liver.

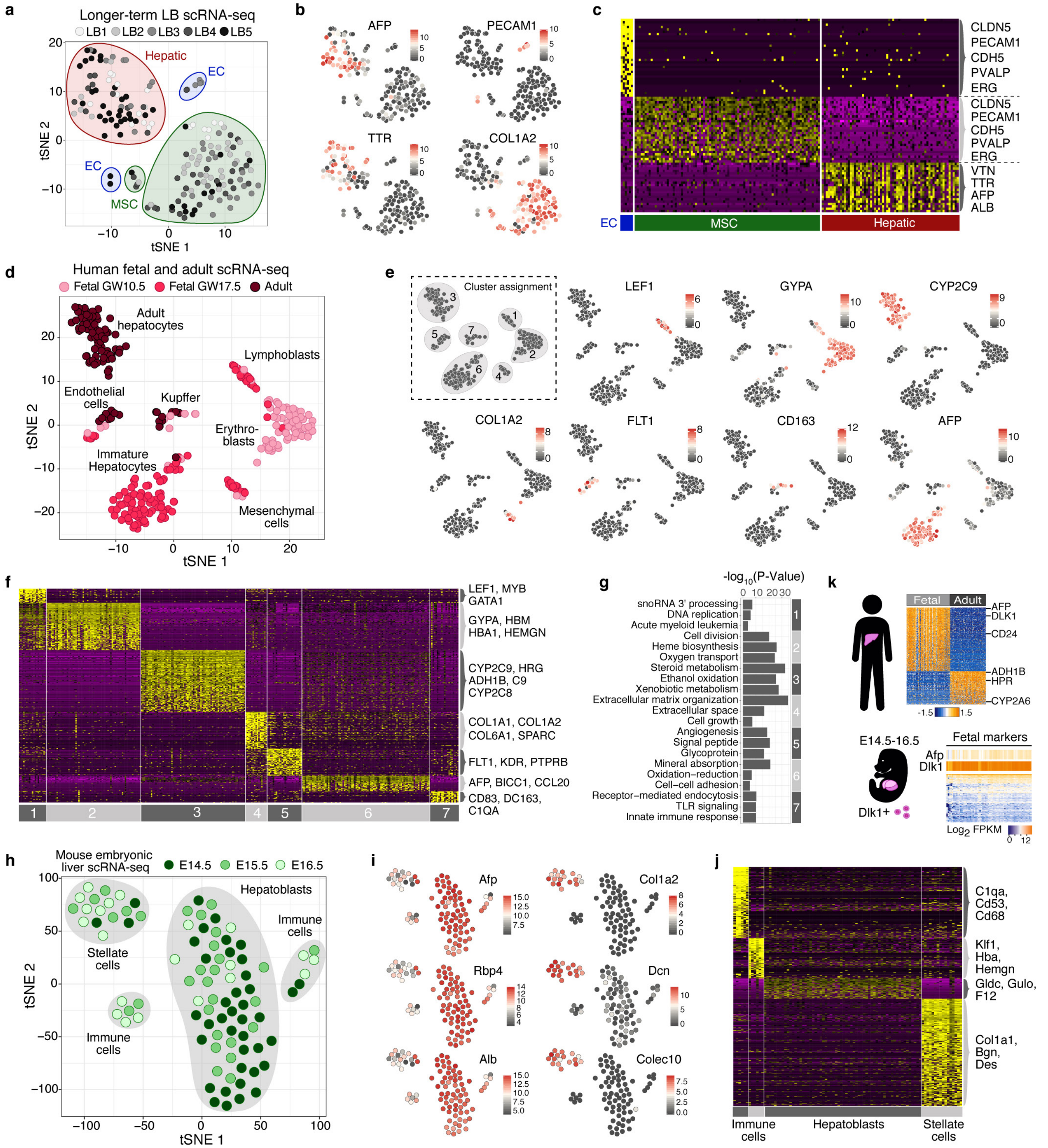

Extended Data Figure 7 | See next page for caption.

Extended Data Figure 7 | Cell composition in human longer-term LBs, adult and fetal human liver, and mouse embryonic liver. a, scRNA-seq was performed on LBs grown for an extended period in culture (LB1 = 11 days in 3D, LB2 = 12 days, LB3 = 7 days, LB4 = 13 days, LB5 = 10 days; 173 cells total). PCA was used to identify genes describing cell populations, and tSNE was used to cluster cells. We identified hepatic, endothelial, and MC clusters. **b**, Expression of genes marking each cluster is coloured ($\log_2$(FPKM scale)). **c**, Scaled heatmap (yellow, high; purple, low) of genes specifically expressed (average difference >2, power to discriminate >0.5) in each cluster (labelled at the bottom), with exemplary genes from each cluster labelled on the right. Cells are in columns, genes in rows. **d**, scRNA-seq was performed on human adult (5 donors, age 21 – 65, 256 cells) and fetal (gestation weeks 10.5 and 17.5, 238 cells) after enrichment for hepatic lineage cells. PCA was used to identify genes describing cell populations, and tSNE was used to cluster cells. We identified hepatic, endothelial, mesenchymal, and immune lineage cells both in fetal and in adult tissues. **e**, Cluster assignments are highlighted on the tSNE plot and expression of genes marking each cluster is coloured ($\log_2$(FPKM scale)). **f**, Scaled heatmap (yellow, high; purple, low) of genes marking each cluster (numbered at the bottom), with exemplary genes from each cluster labelled on the right. Cells are in columns, genes in rows. **g**, Marker genes (average difference >2, power to discriminate cluster >0.5) were analysed for GO enrichments, and representative top enrichments are shown with the *P* value ($-\log_{10}$). **h**, scRNA-seq was performed on mouse hepatoblasts isolated from mouse liver at E14.5, E15.5, and E16.5 (92 cells total). PCA was used to identify genes describing cell populations, and tSNE was used to cluster cells. We identified hepatic, mesenchymal, and immune cell clusters. **i**, Expression of genes marking each cluster is coloured ($\log_2$(FPKM scale)). **j**, Scaled heatmap (yellow, high; purple, low) of genes specifically expressed (average difference >2, power to discriminate >0.5) in each cluster (labelled at the bottom), with exemplary genes from each cluster labelled on the right. Cells are in columns, genes in rows. **k**, Heatmap showing normalized expression (*z*-score) of genes differentially expressed between fetal and adult human hepatocytes. Column, gene; row, cell. Heatmap shows that fetal hepatocyte marker genes are highly expressed in mouse AFP^+, ALB^+, DLK^+ early hepatocytes/hepatoblasts, corroborating the human fetal data.

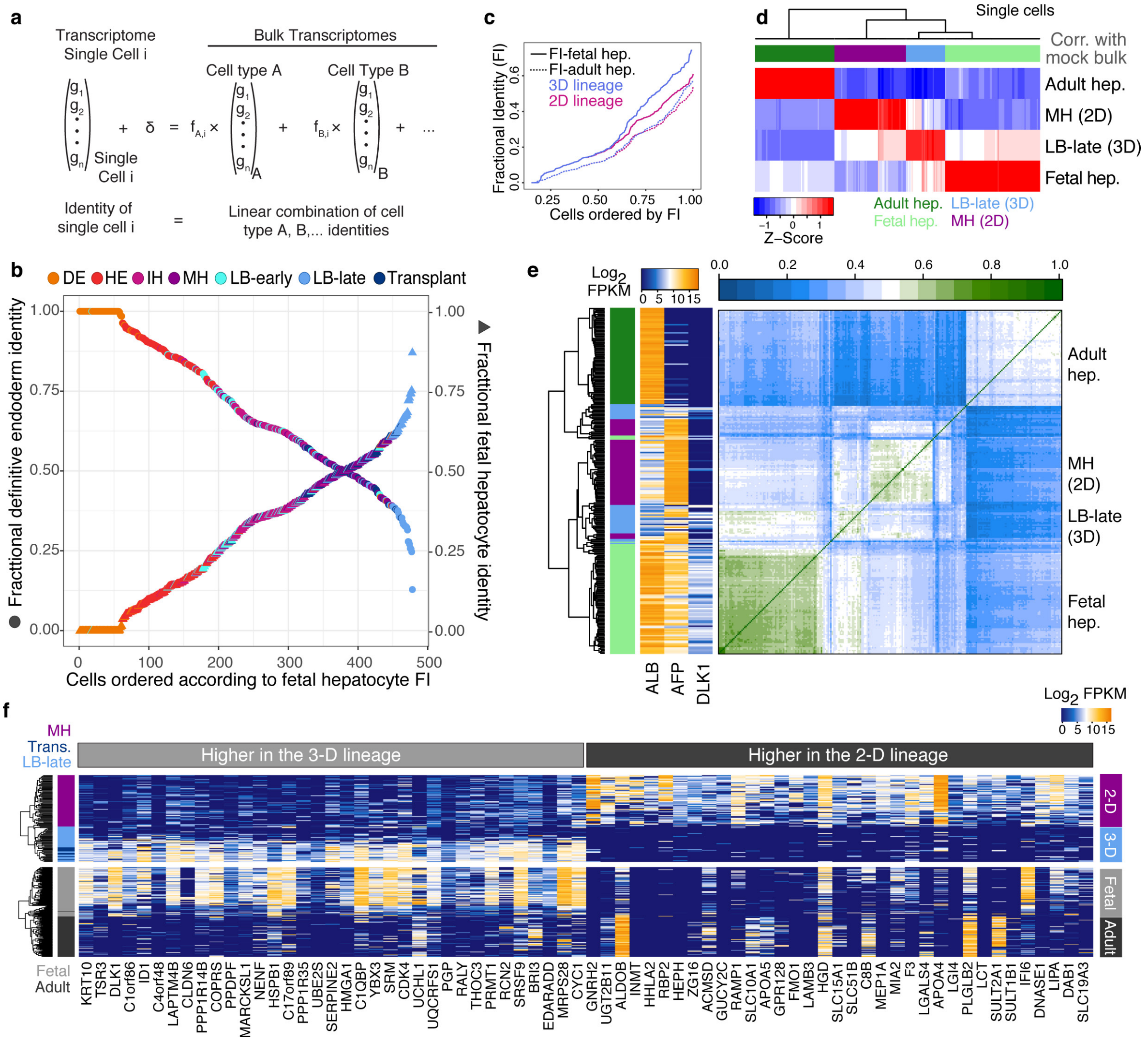

Extended Data Figure 8 | LB hepatic cells resemble human fetal hepatocytes. a, Overview of quadratic programming. Fractional identities are calculated assuming a linear combination of different cell fates. Mock-bulk transcriptomes from DE, fetal hepatocytes, and adult hepatocytes were generated by averaging the single-cell transcriptomes from each group. **b**, For each cell, the similarity to bulk RNA-seq from either DE or fetal hepatocytes was calculated by using quadratic programming and plotted as fractional identities (left axis, circle, fractional DE identity; right axis, triangle, fractional fetal hepatocyte identity). Points are coloured on the basis of the experiment: DE (orange), HE (red), IH (pink), MH (purple), early LB hepatic (LB-early, 3 days, teal), late LB hepatic (LB-late, 5 – 10 days, light blue), and transplanted hepatic (transplant, 5 – 10 days, dark blue). **c**, For all cells on the 2D and 3D lineage, quadratic programming was used to calculate the fractional identity of each cell's transcriptome with mock-bulk transcriptomes from DE or hepatocytes (fetal or adult). Fetal (solid line) and adult (dotted line) hepatocyte fractional identity is plotted for 2D (pink) and 3D (blue) lineage cells ordered in ascending order. Hepatic cells from the LB are the most similar to fetal hepatocytes. **d**, Heatmap shows normalized correlation (*z*-score) of single-cell transcriptomes with mock-bulk RNA-seq data from adult hepatocytes, fetal hepatocytes, hepatic cells from late stage LBs, and 2D MH cells. **e**, Correlogram showing the correlation between cells from different cell populations. The left sidebar shows the expression of ALB, AFP, and DLK1. **f**, Heatmap showing differentially expressed genes between 2D and 3D lineages for ALB^+ cells in MH, late LB hepatic, transplanted hepatic cells (top), and fetal and adult hepatocytes (bottom).

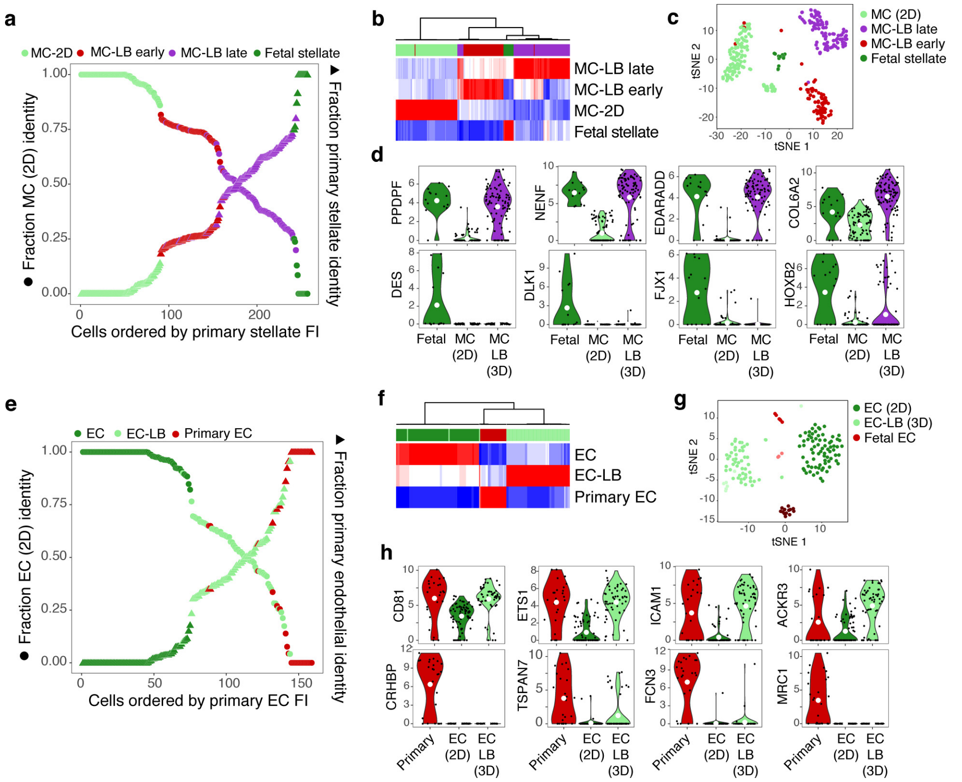

Extended Data Figure 9 | Similarities and differences between endothelial and MCs from the LB and primary human liver. a, For each cell, the similarity to either mock-bulk RNA-seq data from input MSCs grown in 2D culture or primary stellate cells from the fetal liver was calculated using quadratic programming and plotted as fractional identities (left axis, circle, fractional MSC 2D identity; right axis, triangle, fractional stellate identity). Points are coloured on the basis of the experiment: input MSCs in 2D (MSC, light green), MSCs from early LB (MSC-LB early, red), MSCs from late LB (MSC-LB late, purple), primary fetal stellate (fetal stellate, green). **b**, Heatmap shows normalized correlation (*z*-score) of single-cell transcriptomes with mock-bulk RNA-seq data from MSCs from early stage LBs, MSCs from late stage LBs, MSCs grown in 2D, and fetal stellate cells. **c**, tSNE clustering of mesenchymal and stellate cells on the basis of genes identified using PCA. This analysis was used to identify genes specific to fetal stellate cells (Supplementary Table 5). **d**, Violin plots showing the expression distributions of genes similarly and differentially expressed between MSC-LB and fetal stellate cells. White circle, mean. **e**, For each cell, the similarity to either mock-bulk RNA-seq data from input ECs grown in 2D culture or primary ECs from fetal and adult liver was calculated using quadratic programming and plotted as fractional identities (left axis, circle, fractional EC 2D identity; right axis, triangle, fractional primary EC identity). Points are coloured on the basis of the experiment: input ECs in 2D (EC, green), ECs from early LB (EC-LB, red), and primary fetal and adult ECs (primary EC, red). **f**, Heatmap shows normalized correlation (*z*-score) of single-cell transcriptomes with mock-bulk RNA-seq data from ECs grown in 2D, ECs from early stage LBs, and primary liver ECs. **g**, tSNE clustering of ECs on the basis of genes identified using PCA. This analysis was used to identify genes specific to primary liver ECs (Supplementary Table 5). **h**, Violin plots showing the expression distributions of genes similarly and differentially expressed between EC-LB and primary endothelial cells. White circle, mean.

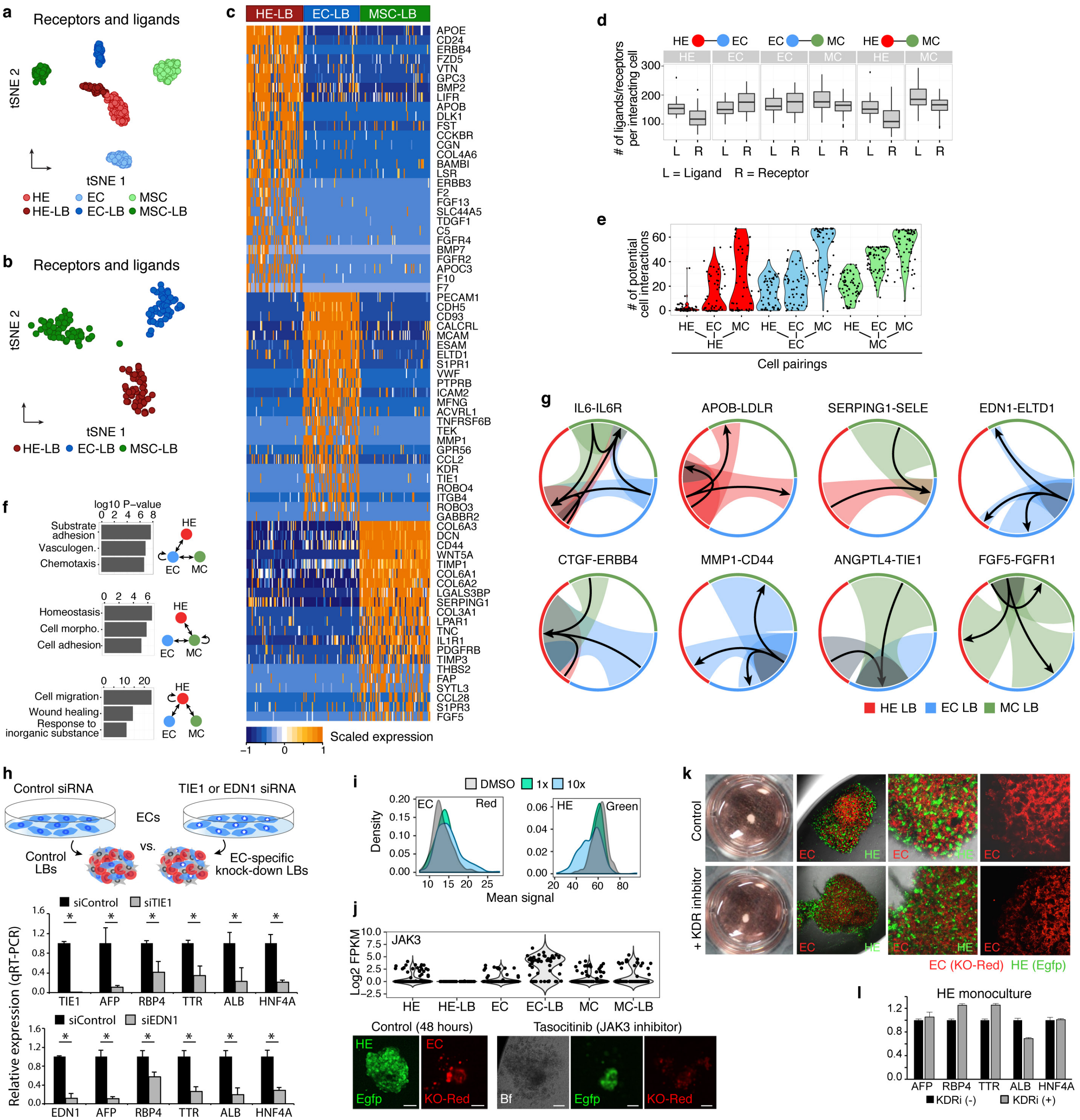

Extended Data Figure 10 | Potential interlineage signalling in LBs. **a**, **b**, t-SNE plots based on the expression of receptors and ligands show that input and LB cells cluster separately. **c**, Heatmap shows the scaled expression of receptors and ligands differentially expressed between HE, EC, and MC cells in the early LB. **d**, Boxplots show the number of ligands (L) or receptors (R) for each lineage combination. For example, hepatoblasts average 150 ligands and 100 receptors for every HE–EC interaction. **e**, Violin jitter plots showing the number of potential cell interactions for each lineage combination calculated from the network shown in **b**. **f**, Top GO enrichments and *P* values for receptor–ligand pairings where one of the three cell types (EC, MC, or HE) are required for the interaction. **g**, Each of the three LB lineages (HE, red; EC, green; MC, blue) are represented as a third of the circle. The fraction of cells expressing mRNA for each ligand is highlighted and linked to the fraction of cells expressing the receptor. The arrows designate the direction of the link (ligand to receptor). A subset of cells may express both receptor and ligand and are shaded accordingly. **h**, qRT–PCR for hepatoblast marker genes shows that hepatic differentiation is impaired in LBs generated from ECs with knockdown of an endothelial specific receptor, TIE1 (top), or endothelial specific ligand, EDN1 (bottom). LBs were generated containing TIE1 or EDN1 knockdown ECs, combined with normal wild-type HEs and MCs. Two-sided *t*-test, $^*P < 0.05$; error bars, s.d. Data from three independent differentiations. **i**, Distributions of mean fluorescence intensities from maximum projections of each micro-LB in the green (hepatic) and red (endothelial) channels. These signals were used to calculate a hepatic-to-endothelial signal ratio for each micro-LB. **j**, Top: violin plot showing the expression distributions of JAK3 expression across input and early LB cell types. Bottom: representative maximum projection images of a micro-LB at the 48 h time point from a DMSO-treated control and with 10 μM tasocitinib, an inhibitor targeting JAK3 of the JAK/STAT pathway. **k**, Addition of KDR/VEGFR2 inhibitor (SU1498) does not affect the self-condensation process; however, endothelial sprouting is impaired in the presence of KDR inhibitor. **l**, qRT–PCR for hepatoblast marker genes shows that hepatic differentiation is not significantly impaired in HE monoculture in the presence of KDR inhibitor. Error bars, s.d. Data from three independent differentiations.